UCLouvain

École polytechnique de Louvain

Porous silicon Bragg flakes towards optical sensing

Author: **Antoine DE LA VALLÉE POUSSIN**
Supervisor: **Laurent FRANCIS**
Readers: **Jean-Pierre RASKIN, Sorin MELINTE**
Academic year 2024–2025
Master [120] in Physical Engineering

Abstract

Porous silicon (PSi) is a composite material that is known for its simplicity and versatility. There are numerous applications, including optical sensing. An optical sensor using a porous silicon part can be improved with the presence of a Bragg stack at the surface, made in the same material.

In this work a production process including electroetching is used to create a free-standing PSi membrane, or flake. The optical properties are enhanced by the presence of a Bragg stack on one side. The process is compatible with microfabrication techniques used for semiconductors.

The validity and reproducibility of the production process are evaluated in this work. A numerical model is used to better analyse the optical properties of the flake. Different reflecting samples were made and characterized. Their optical properties are measured and compared to the model. Some improvements on the methodology used to characterize the optical properties of the samples were proposed, with a significant noise reduction with these samples.

The application in a sensing device is also discussed. Although the sensing response is not yet accurate, the results provide valuable insight into the limitations of the current procedure and suggest possible improvements for future research.

While there is still room for improvement in the production and characterization processes, these samples may be used effectively in the future, for chemical or biosensing applications.

Acknowledgements

This work could not have been possible without the help of other people. Therefore, I would first like to thank Laurent Francis, for the supervision of this work, his advice and for the interesting discussions we had at different stages of this work.

I also thank my mentor, Romain Hanus, for his guidance at different steps of this work. I am grateful for the time he has taken to introduce me to the labs (fabrication) and to various methods of characterizations of PSi membranes, and for helping me understand different microfabrication techniques and the complex physics and technical challenges related to PSi ion membranes.

I express my gratitude to Clémentine Gevers for introducing me to the physics of Bragg reflector and to optical characterization (reflectometry), and for her help with the work in clean room. Her advice was very helpful for adapting the numerical model, for the structuration of this work and for interpreting the results.

I am also grateful to Delphine Magnin and Armand Beche for helping me to get some great scanning electron microscope (SEM) images and energy dispersive X-ray (EDX) analysis. These were very useful for the first part of this work, to validate and get a better understanding of some fabrication methods.

A great thank to Clara Whyte Ferreira for her advices for improving the optical measurements. These were extremely helpful in the last part of this work.

Finally, I would also like to thank the staff at Winfab for their kindness and readiness to help during my laboratory work.

Contents

List of Tables

List of Figures

Acronyms

CRI complex refractive index.

EDX energy dispersive X-ray.

EOT effective optical thickness.

LLL Landau-Lifshitz-Looyenga.

PSi porous silicon.

RMS root mean squared.

SEM scanning electron microscope.

SLIM Spectroscopic Liquid Infiltration Method.

SNR signal-to-noise ratio.

TMM transfer matrix method.

Chapter 1

Introduction

1.1 Context and structure

Porous silicon (PSi) is a composite material that has attracted a lot of attention since the 1990's. It shows interesting properties such as luminescence or large surface inside the pores. This material has a large number of applications, including sensing, drug delivery or opto-electronics. [12][41] The application that motivated this work is optical sensing. The production of a PSi Bragg reflector seems interesting for this application.

A method for the production of a reflecting PSi membrane is presented. The purpose of this work is to produce a few membranes, measure their properties and discuss the results. Data from the literature and numerical models are used for interpreting the measurements.

The subject of this work is detailed in a first chapter. The context of this work and previous results from the litterature are first exposed. The purpose of this work is then explained and justified with these results.

The physics that explains the optical properties are presented in a second chapter. Different approaches are presented for the computation of the refractive index of porous silicon. A method is presented to estimate the parameters for the fabrication and a more complex model is presented and used to compute the reflectance of the membrane. A discussion on the theoretical response to the change in the environment is also presented.

The next part presents the experiments. First, the production process and optical characterization are presented. Different samples were made with the same technique described. The different steps for the fabrication are presented. Samples with different thicknesses of the reflective layers were made. The reflectance of these different samples are measured then compared, and an estimation of the uncertainty on these results is presented.

The results are then compared to the model. Different sources of error are identified in the experimental setup. Some limitations of the physical model are also identified. The use of this structure for optical sensing is also discussed in this part. The samples have shown interesting results for optical sensing because of their good sensitivity, simplicity and adaptability, but the reproducibility and sensitivity could be improved. Therefore, some possible improvements on the design, production and measurements are also discussed in this part.

The last chapter concludes and presents a summary of the process, results and future perspectives.

We only consider one type of membrane in this work. But a different type of membrane, with a different shape or with different materials, might perform better. The optimizations and limitations presented here should also be taken into account when using a different design.

1.2 State of the art

1.2.1 Porous silicon

"Porous silicon is a sponge-like structure of monocrystalline silicon which although accidentally discovered, soon became one of the most well-researched silicon structures." [15]

PSi can also be described as a nanostructured composite material of air and silicon. The pores inside this structure can be very dense or sparse, and have various sizes and shapes. [15]

Fabrication

Various techniques can be used to produce a porous structure from a silicon substrate. Physical etching or chemical etching can be used. Physical etching methods include reactive-ion etching, spark erosion or laser-induced plasma erosion. Chemical etching methods include electrochemical etching, strain etching, photoetching or metal-assisted etching. Chemical etching methods can produce a structure with pores sizes ranging from a few nm to a few microns. Substrates with different crystallinity, doping and crystal orientation can be used. This choice will affect the reactions occurring at the surface. [16]

Only electrochemical etching is considered in this work. The setup is presented in section 3.1.1. Different parameters can be used to control the shape of the porous structure. The concentration of the etching solution, the solvent, and the applied current determine the porosity and etch rate. [35]

Properties

The bulk silicon is a brittle semiconductor with a band gap of 1.1 eV. It is very reactive and a thin layer of silicon dioxide is formed during the process or upon exposure to the air. [2] PSi is lighter and more fragile. There are different types of porous structure with different pores sizes: [35]

- microporous, with pore diameter lower than 2 nm
- mesoporous, with pore diameter ranging from 2 to 50 nm
- macroporous, with pore diameter larger than 50 nm

This material has a high surface area, which makes it interesting for sensing applications. A surface of 100-800 m^2/g were reported for mesoporous structures. [16][23]

PSi is also biocompatible, and applications of this material for in vivo electronics has been investigated. [41]

Luminescence and quantum confinment were also observed in PSi since the 1990's. Stable luminescent structure can be produced with this material. The luminescence and the band gap of the structure changes with the porosity. [4][35][24]

Other optical properties change with the porosity. The permittivity can be tuned, with applications for radio-frequency devices. [36] The refractive index can vary between 1 and 4 while the absorption coefficient stays between 0 and 10^5 cm^{-1} in the visible spectrum (see section 2).

PSi nano particles can be produced. They can have different chemical and physical properties, making them more suitable for other applications. For instance, these can be more suitable for biomedical applications. [48]

Because of their various properties and fabrication techniques, PSi has been used for many applications, including energetics, electronic devices, electro-optics, chemical or biosensing. [29][18][21][12][3][23][8]

PSi membranes

Because of its interesting properties, PSi can be used in different types of devices. This material has applications in the field of biomedicine, sensors, solar cells, electrochemical energetics, and microelectronics. [44] [20]

Some fluid can go through this material once the bulk silicon below the porous structure is etched out. A measurement can be made on these membranes with a flow-through setup. Therefore, a membrane made out of this material is particularly suitable for sensing or interacting with a fluid. [44] The applications for PSi used as an ion membrane were also investigated.

Different types of ion membranes can be produced: anion- or cation-echange membranes, amphoteric membranes, or bipolar membranes. [14] There are various applications for these membranes, including ion sensing, energy conversion, iontronic devices or water treatment. [1][9][26] The main physical principles used in these applications are the following. [14]

- Electrodialysis
- Diffusion dialysis
- Membrane capacitive deionization
- Reverse electrodialysis
- Fuel cell
- Redox flow battery
- Electrolysis

However, porous membranes containing only silicon did not seem to fit the main applications for this type of membranes, because of a low permselectivity. Modified membranes, produced with the deposition of another material, showed better performance and seems more suitable for the production of ion membranes. [13][29] For now, these membranes should be more suited for other applications like environment or biosensing.

Pure silicon is not stable, in particular in an aqueous medium. Different techniques can be used to modify the surface properties and reduce the degradation of the membrane in an aqueous medium, like oxidation, silanization, hydrocarbonization or atomic layer deposition. [47] This step is necessary because the membrane we produce should work in an acqueous environment. It is less compatible with biomedical applications otherwise. Changing the surface properties also extends the number of applications for chemical or biosensing. For example, the surface can be activated for the selective detection of particular chemical or biological species. [3]

1.2.2 Bragg mirror

Iridescence is a well-known effect in nature. Some animals have a thin layer at the surface of their body coated with reflectin, a layer that reflects very well the light in a specific range of wavelengths. For example, some bird feathers, butterfly wings, and fish scales are colored and reflect light using this effect. And some cephalopods use this as a camouflage or mean of communication. A Bragg mirror is an artificial structure that also shows iridescence. [40]

A Bragg mirror, is a unidimentional structure made of a stack of thin layers, alternating between a high and low refractive index. It can reflect an electromagnetic wave that has a high reflectivity around a target wavelength λ_T. Its reflectivity around λ_T can reach values higher than 99%. It is sometimes called a dielectric mirror because it was initially made using dielectric materials: oxide, nitride or fluoride compounds (e.g.: SiO_2/TiO_2 mirrors). Semiconductors are also used for the fabrication of Bragg mirrors (e.g.: $AlGaAs/GaAs$ mirrors). As a consequence, these mirrors can have a significant electrical and thermal conductivity. [25][49]

Different methods can be used to make these multilayered stacks. Solution-based methods include spin-coating, dip coating and doctor blading. These methods are cheap, and allow to deposit organic polymers, but are not very accurate, as Bragg mirrors made this way have a reflectance rarely exceeding 95 %. [27] More common fabrication methods are electron beam deposition, ion assisted deposition, ion beam sputtering, plasma-based film deposition or epitaxial growth. A reflectivity larger than 99 %

is necessary for some applications like laser cavities. However, this level of reflectivity can't be reached with standard metallic mirrors, like those made of a silver film. High quality Bragg mirrors are thus needed in these cases. [25][49]

A reflector that includes air gaps have also been investigated. These are particularly interesting because of the refractive index of air, that is lower than for other materials (the computation of optimal indices is presented in section 2). However, the low electrical and thermal conductivity makes it less suitable for electrical devices. [49]

Another type of reflector without these drawbacks is a reflector with a semiconducting porous structure. A reflectivity larger than 99.5 % has been reported for a nanoporous n-doped GaN structure. [49]

Other porous semiconductors can be used. For a silicon Bragg stack, a silicon wafer is etched, producing a porous structure with variable porosity. This structure is then heated. The resulting material is a hybrid porous structure containing silicon and silicon oxide. The fabrication process is relatively cheap and compatible with IC fabrication techniques. Reflectance values can reach 90 %, or even more when the fabrication is made at low temperature. [22][38]

1.2.3 Context of this work

A single layer of a porous material can be characterized using Spectroscopic Liquid Infiltration Method (SLIM) method. This method uses the relation that exists between the fringes observed in the spectrum of the reflectance (measured at different wavelength) and the effective optical thickness (EOT). The EOT depends on the properties of the layer and of the medium inside the pores. The inverse method can be used to characterize a fluid that is present inside the pores. [11][33]

In the same way, a Bragg stack can be characterized with the SLIM method. [45] The change in EOT induces a shift of the peaks in the reflectance spectrum. For this type of reflector, the shift in wavelength is used instead of the fringes in the reflectance spectrum.

A Bragg stack made out of a porous structure can also be used for sensing a medium. For example, a Bragg stack in PSi could be used for biosensing. A previous study showed interesting results for bacterial lysate detection, with a much lower detection limit than for single layer SLIM. [10] It used a lateral flow of liquid, going through the sample. The samples showed a maximum reflectance between 40 and 95 %. Compared to its numerical model, this study showed a good reflectivity but bad accuracy for the peak wavelength with a highly porous structure, and a better accuracy with low reflectivity using a less porous Bragg stack.

The goal of this work is to study the possibility of producing a similar mirror on top of a PSi flake. These flakes should be suited for the characterization of a solution by measuring a change of refractive index. Their optical properties are discussed, as well as their optical response in presence of a different fluid. An experimental setup for the characterisation of its optical properties is proposed and its application as an optical sensor is discussed.

This work also involves some simulations with a numerical model. This model was used to estimate the best porosity, and geometry for the reflector. It also served as a reference for the interpretation of the measurements and helped to identify the parameters of interest of the membrane (used to compare the optical properties of different samples). The experiments and measurements are used to validate the numerical model.

With better performance, these membranes could become affordable and reliable sensors, with a high societal impact. They could save the lives of thousands of people, by detecting the presence of pathogens such as bacteria or parasites. [10][17]

Chapter 2

Physical models

2.1 Bragg mirror

A Bragg mirror is a stack of thin layers alternating with a high and low refractive index, used to reflect an electromagnetic beam that has a wavelength in a given range. A part of the beam can be reflected or transmitted at the interface between each layer. This is illustrated on figure 2.1. The interferences between the reflected beams produce a reflectance spectrum that oscillates with the wavelength.

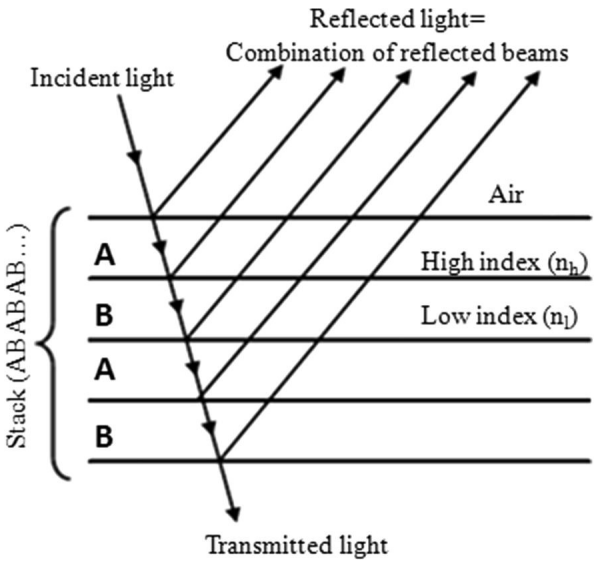

Figure 2.1: Illustration of a multilayered stack of a Bragg mirror and the reflection of the incident beam (going downwards) at each interface. [43]

Let us consider a Bragg stack in a homogeneous medium (air), and an electromagnetic wave traveling perpendicular to the layers of the stack. The following section describes the physical model used to compute the fraction of the incident power that is reflected or transmitted through the stack. [7]

2.2 Transfer matrix method

When a beam of light reaches an interface between 2 media with refractive indices n_i and n_{i+1}, this beam is partially reflected at the interface. The Fresnel equations give the amplitude of the beam that is reflected (r) or transmitted (t). The reflection and transmission are represented in figure 2.2. It depends on the refractive indices n_i and n_{i+1}. The fraction of the transmitted (reflected) beam is written t_1 ($r1$) or t_2 (r_2) depending on the direction of the incident beam.

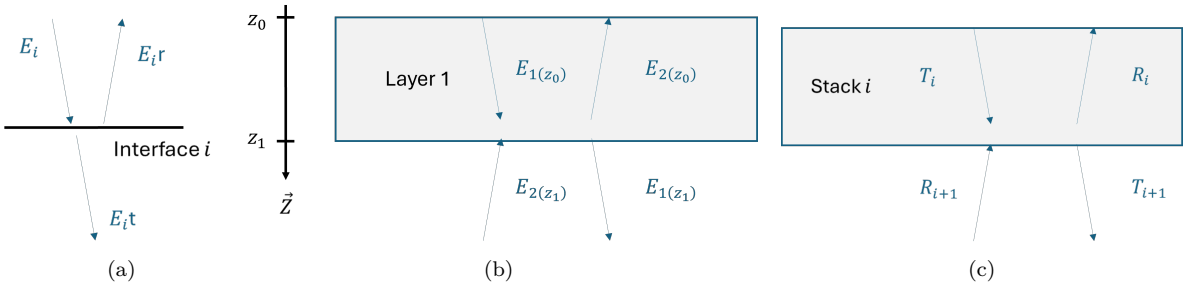

Figure 2.2: Illustration of the unidimensional reflection and transmission of electromagnetic beam in an inhomogeneous medium:
(a) amplitude of the electric field at an interface between 2 media.
(b) amplitude of the electromagnetic beam traveling in both directions (perpendicular to the plane of the 2 interfaces, along $\vec{Z}$ and $-\vec{Z}$ directions), on each side of a thin layer.
(c) transmitted and refracted power on each side of a multilayered stack. The light is coherent in the stack, but incoherent in the 2 layers above and below the stack.

When an electromagnetic wave goes through a material with the refractive index n, its phase changes with the distance z and time t. The beam is partly absorbed in the material and its amplitude decreases inside the material with the distance that the beam travels. The change in phase and amplitude in a material are described with the complex refractive index $\tilde{n} = n + \kappa\, i$ and the wavelength of the wave λ.

If the initial amplitude of the transmitted wave is $E_{1(0)}$ and the extinction coefficient (imaginary part of the refractive index) is κ, the amplitude decreases exponentially with the distance z.

$$E_{1(z)} = E_{1(0)} \exp\left(-\frac{2\pi}{\lambda}\kappa z\right) \tag{2.1}$$

The attenuation coefficient is defined as $\alpha = \frac{4\pi}{\lambda}\kappa$. The initial transmitted power is written T_0 and the transmitted power also decreases exponentially with space.

$$T = T_0 \exp(-\alpha z) \tag{2.2}$$

Let us consider a thin layer with a different refractive index (n_1) than its environment (n_0), illustrated in figure 2.2. Reflection and transmission can occur on both sides of this layer. Therefore, we consider a beam going downwards, with amplitude E_1, and a beam going upwards with amplitude E_2. These amplitudes can have different values at each interface.

The transmission and reflection of a beam can be described with a transfer matrix M, with the following relation. Different notations are used to describe the amplitude of the electric field. These are represented in figure 2.2.

$$\begin{bmatrix} E_{1(z_1)} \\ E_{2(z_1)} \end{bmatrix} = M \begin{bmatrix} E_{1(z_0)} \\ E_{2(z_0)} \end{bmatrix} \tag{2.3}$$

where

$$M_{(z_0,z_1,\tilde{n}_0,\tilde{n}_1)} = \begin{bmatrix} M_{11} & M_{12} \\ M_{21} & M_{22} \end{bmatrix}$$

This matrix can be defined using the values of Fresnel coefficients at the interfaces, wavelength, complex refractive index of the material and geometry (thickness of the layer).

For a material made up of a stack of N layers, the resulting transfer matrix M can be computed. It corresponds to the product of transfer matrices defined for each interface (M_0) or layer M_i.

$$M = M_0 \prod_{layer\ i} M_i \tag{2.4}$$

Computing the elements of the matrix M is very useful in this work because the equivalent reflectance (or reflected power) R and transmittance (or transmitted power) T can be computed from these. R and T are defined with respect to the incident power and have a value between 0 and 1.

$$r = \frac{M_{21}}{M_{11}} \tag{2.5}$$

$$t = \frac{1}{M_{11}} \tag{2.6}$$

$$R = |r|^2 \tag{2.7}$$

$$T = C|t|^2 \tag{2.8}$$

If n_0 and n_f are the refractive indices of the medium before and after the whole set of layers that is modeled (the whole flake), the correcting factor for the transmittance is simply $C = \frac{n_f}{n_0}$. The value $C = 1$ will be use since our tests are carried out in a homogeneous environment.

In our design, a thick layer is used as a support for the Bragg stack. The thickness is much larger than the wavelength and the coherence of the light beam is lost in this layer. The previous development does not account for incoherence. But the decreasing intensity can be taken into account in this model. In order to model incoherent layers, one must define some values of reflectance or transmittance R_i and T_i between each of these incoherent layers. 2 incoherent layers separated by a coherent stack are illustrated in figure 2.2. A transfer matrix M' can be defined for the first interface or for a single incoherent layer:

$$\begin{bmatrix} T_{(z_1)} \\ R_{(z_1)} \end{bmatrix} = M' \begin{bmatrix} T_{(z_0)} \\ R_{(z_0)} \end{bmatrix} \tag{2.9}$$

The matrix M' can be defined using the wavelength, complex refractive index of the material, geometry and reflectance and transmittance of the coherent stack (or interface) between 2 incoherent layer. Reflectance and transmittance of the coherent stack are defined in both directions.

In figure 2.2, these correspond to $\vec{Z}$ and $-\vec{Z}$. The equivalent transfer matrix for the Bragg stack and the support layer is then computed with a matrix product of local transfer matrices:

$$M' = M'_{stack} M'_{support\ layer} \tag{2.10}$$

The equivalent reflectance and transmittance can then be computed.

$$R = \frac{M'_{21}}{M'_{11}} \tag{2.11}$$

$$T = \frac{1}{M'_{11}} \tag{2.12}$$

A Python code has been written to simulate the values of R and T for the whole flake. The Python library tmmpy also implements the transfer matrix method (TMM) in a more general case, and was used to check the results. [7]

2.3 Optical properties

Porous silicon is a composite of silicon and air. In order to model the reflectance of the surface of a multilayered porous silicon, the values of refractive index and extinction coefficient of each layer are required. These values change with the wavelength of the incident ray λ.

For a pure material (air, silicon), the values $n_{(\lambda)}$ and $\kappa_{(\lambda)}$ are found directly in the literature. [30] The values used and their dependence on the wavelength are represented in figure 2.3.

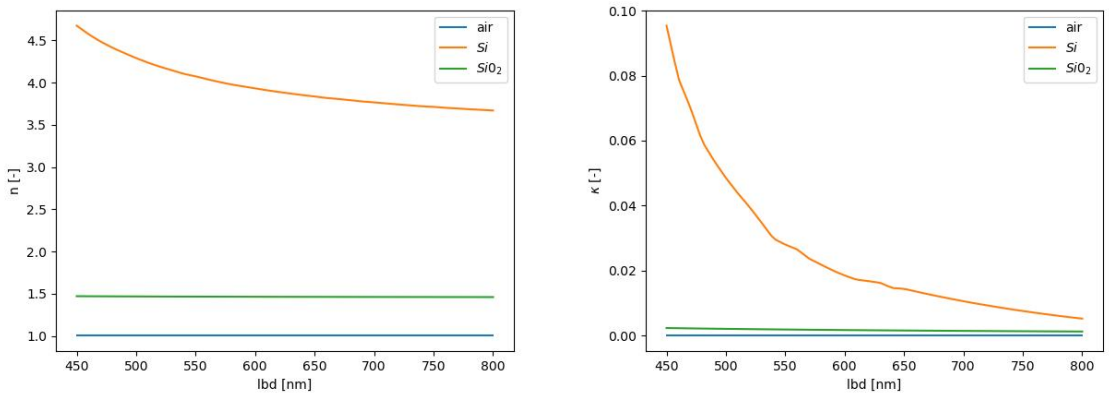

(a) (b)

Figure 2.3: Representation of the refractive index n and extinction coefficient κ for different materials, considering wavelengths between 450 and 800 nm.

For a porous structure or a heterogeneous mix of different materials, different models can be used to estimate the optical parameters. [5]

- Mean-field models, based on the laws of electromagnetism
- Mixing rules
- Empirical relationships

One effective medium theory (or mean-field) model is the Bruggeman's model. Let us consider a mix of 2 homogeneous materials, with dielectric constant ϵ_1 and ϵ_2, and a relative volume for the first one r_v. The equivalent dielectric constant ϵ is expressed as the following expression, with $H_b = (3r_v - 1)\epsilon_1 + (2 - 3r_v)\epsilon_2$ and ϵ chosen such that its real (and imaginary) parts are positive. [6]

$$2\epsilon^2 - H_b\epsilon - \epsilon_1\epsilon_2 = 0 \tag{2.13}$$

The effective dielectric constant for a mix of more than 2 materials can be found by applying the previous formula several times.

For a mix a m constituents, ϵ_i is defined as the permittivity of the constituents i. ϕ_i is its volume fraction and the parameter β is between -1 and 1. The Lichteneker-Rother equation, general formula for the mixing rules, can also be used to compute the effective permittivity ϵ:

$$\epsilon^\beta = \sum_{i=1}^{m} \phi_i \epsilon_i^\beta \tag{2.14}$$

The complex refractive index (CRI) model is found by setting this coefficient β to 0.5. [5] The Looyenga model, or Landau-Lifshitz-Looyenga (LLL) model, is found by setting the parameter β to $\frac{3}{2}$. [37]

The refractive index, relative speed of light in the medium (c_m), compared to the speed of light in the vacuum (c_0), can be deduced from the permittivity for a non-magnetic medium.

$$n = \frac{c_m}{c_0} = \sqrt{\frac{\epsilon\mu}{\epsilon_0\mu_0}} = \sqrt{\frac{\epsilon}{\epsilon_0}} \tag{2.15}$$

In this case, the LLL model should be more appropriate [32] and will be used along with the TMM, in order to simulate the reflectance of the Bragg mirror. The oxidation of the silicon is not taken into account at this point. The values of the real and imaginary part of the complex refractive index of porous silicon, for a chosen wavelength can then be computed. A comparison of these values for a wavelength $\lambda_T = 633$ nm is represented in figure 2.4.

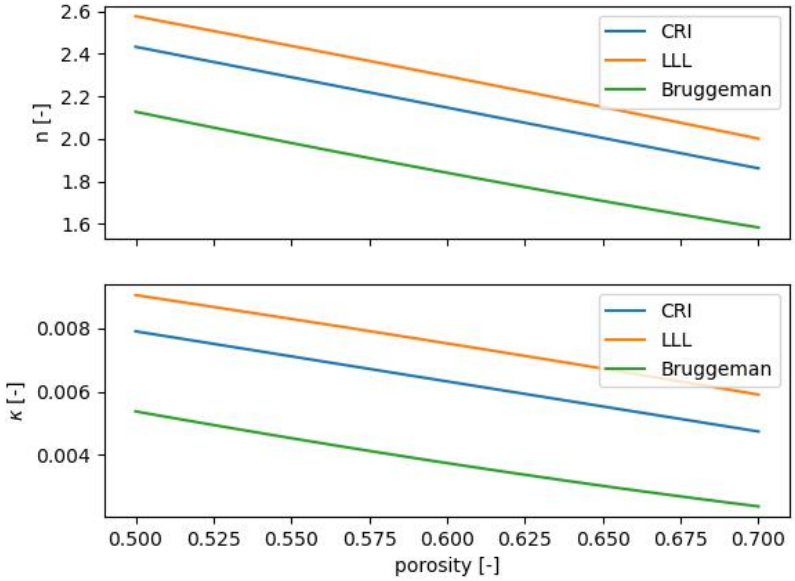

Figure 2.4: Comparison of the complex refractive index $\tilde{n} = n + \kappa i$ found for porous silicon, using 3 different models. The porosity of this material ranges from 50 to 70 %.

2.4 Designing a Bragg mirror

The method used to desgn a Bragg mirror out of oxidized porous silicon is the following.

First, a target wavelength $\lambda_T = 633$ nm is chosen. The reflectance must be higher when the wavelength of the incident beam λ is close to this value. The thickness of each layer (t_A for layers A or t_B for layers B) is chosen such that the EOT is the same in both layers. As a reminder, layers A and B are the 2 types of layers present in a Bragg stack (see figure 2.1).

$$\frac{\lambda_T}{4} = n_A t_A = n_B t_B \tag{2.16}$$

The reflectance is then optimized, using an optimizer in Python (scipy.optimize). [46] The reflectance at the target wavelength R_T is estimated using the values of the number of layers cells N and refractive

indices. Each cell of the stack is made of 2 layers, with refractive index n_A or n_B. This approximation does not take into account the absorption of the beam but is useful to see how the refractive indices and number of layers change the value of R_T and is much faster to compute than TMM. [43]

$$R_T = \left(\frac{(\frac{n_A}{n_B})^{2N} - 1}{(\frac{n_A}{n_B})^{2N} + 1} \right)^2 \tag{2.17}$$

Considering the previous values for the thickness of each layer of the stack, the width of the peak of reflectance around the target wavelength can also be estimated with the following analytical formula.

$$\Delta\lambda = \frac{4\lambda}{\pi}(\frac{n_A - n_B}{n_A + n_B}) \tag{2.18}$$

The values of n_A and n_B are chosen in such a way that the reflectance R_T is maximized in the range of acceptable values (corresponding to porous silicon, with a porosity between 50 and 70 %). The associated refractive indices are computed using the development from section 2.3.

Equation 2.17 shows that the value of R_T increases with the ratio $\frac{n_A}{n_B}$, or when n_A is large compared to n_B. The width of the high reflectance peak also increases when n_A is large and n_B is low. Therefore, for a good reflector, one should maximize the first refractive index and minimize the second. The refractive index tend to decrease with the porosity (going to 1, the refractive index of air, when the porosity tends towards 100 %). This is illustrated in figure 2.4. Therefore, the layers A (high refractive index) are always chosen with the lowest porosity and the layers B (low refractive index) are always chosen with the highest porosity.

Then, the number of cells N is imposed such that the wave transmission through the mirror is lower than 5 % when $\lambda = \lambda_T$. The minimum value that is found for N is $N_{min} = 9$ and the value $N = 10$ will be imposed.

The values found after optimization are presented in table 2.1.

n_A	n_B	ρ_A	ρ_B	t_A	t_B	N
2.58	2	50 %	70 %	61.4 nm	79.1 nm	10

Table 2.1: Values of the parameters of a Bragg stack, for an optimal reflection of the incoming wave, considering a wavelength $\lambda = 633$ nm.

Finally, the transmission spectrum for $\lambda \in [450; 800]$ nm can be computed using the TMM (described in section 2.2). The parameters n_A, n_B, t_A, t_B and N are then used for the fabrication of the porous silicon mirror.

2.5 Sensitivity

When a beam of light travels in the direction of the sample, part of the incident power is reflected, another part is transmitted through the material. These ratios (transmittance and reflectance) depend on the wavelength and are used to describe the optical properties of the sample. The medium inside the porous structure change its refractive index. The reflectance spectra are first computed numerically, considering different filling media.

The fluid in the structure is characterized by its refractive index at the target wavelength. The changes observed in the spectrum are then discussed and compared to the optical properties of the filling medium. Figure 2.5 shows that the presence of a material in the pores that replaces air reduces

the peak reflectance, and induces a red-shift.

The expression of the shift in wavelength in different media of refractive index n_{fill} is difficult to compute analytically. However, figure 2.5 shows that the trend is roughly linear in the range presented here. The sensitivity, defined as the ratio between the variation of the shift of the peak and the variation of n_{fill}, can then be computed. This model predicts a value around 120 nm^{-1}.

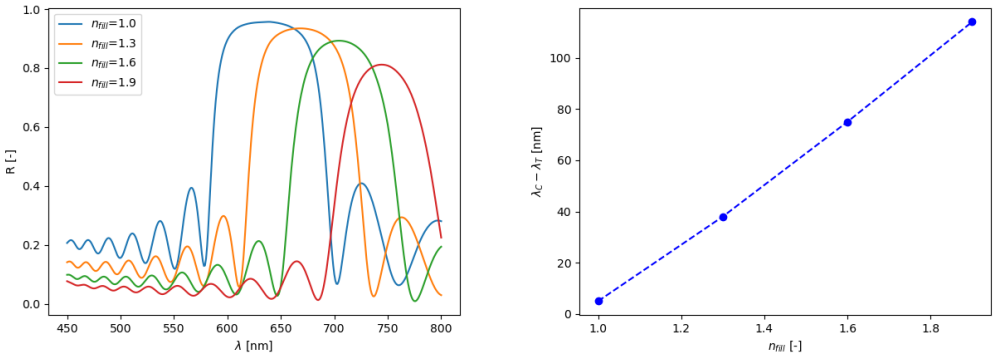

(a) (b)

Figure 2.5: (a) Reflectance spectra of the flake computed considering different filling media (air or a liquid) and (b) shift of the peak compared to the target value in each case. The method used to compute the position (center wavelength) of the peak of reflectance is presented in section 3.2.6.

Chapter 3

Experimental methods and results

3.1 Fabrication process

3.1.1 Electroetching

The flakes were produced from boron-doped (p-type) silicon wafers, with a resistivity of 1 $m\Omega\ cm$. During the etching process, the top surface of the wafer is placed in an electric field, and in contact with a solution of hydrofluoric acid (HF). A platinum electrode (anode) is placed inside the solution and an aluminum foil (cathode) is in contact with the lower surface of the wafer. These are used to impose the electric field. A schematic of these different parts is presented in figure 3.1 Fluorine ions (F^-) present in the solution react with the silicon to create silicon hexafluoride that can diffuse in the solution. The solution used is a mix of HF (49 %) and ethanol 3:1.

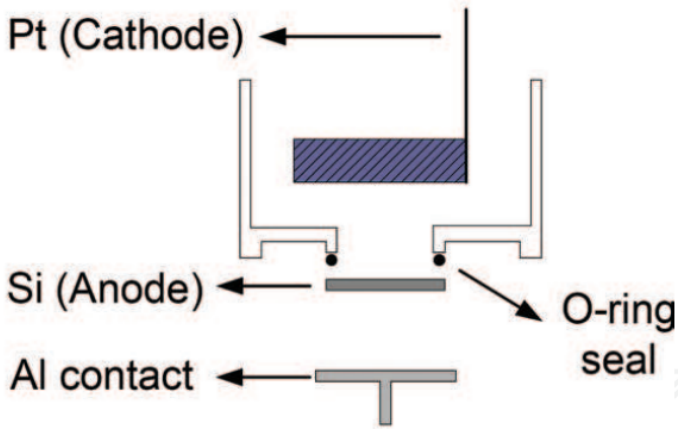

Figure 3.1: Representation of the different components used for the etching process. [15]

The electric field generates a local reaction with the fluorine ions, producing a porous structure. This process has already been described in different papers. [20] [35] The porosity, pore size or etching speed can be controlled with the electric field. The setup used for the porosification is the same as that used in some other papers, [33] and the surface of silicon that is exposed to the etching solution is more or less 0.27 cm^2.

The etching process of the porous silicon flakes contains 3 different steps that are described here.

Sacrificial layer

The surface of the wafer is first etched during 30 second in the HF solution. The etching occurs in the presence of an electric field imposed by a current source. The target current is the same as used in the next step (32.7 mA/cm^2). Then the surface is rinsed with isopropanol (IPA) and immersed in a solution of KOH (1M) during 2-3 minutes. This removes a thin layer on the surface, creating a rough surface. This step is important to avoid the presence of a thin transitional layer with different pore sizes on top of the sample. [33] [10]

Porosification

After removal of the sacrificial layer, the substrate is etched, in order to get the porosity required for the flake that is produced. A current source (a Keithley 2460) imposes a constant current through the etching solution and the substrate.

The porosity p of the resulting porous silicon increases with the applied current density J. The relation between porosity and current density is presented in figure 3.2. These values depend on the electrical properties of wafer. The trend $p_{(J)}$ was approximated by linear segments and this function was reversed. The current density could then be chosen in order to match the required porosity.

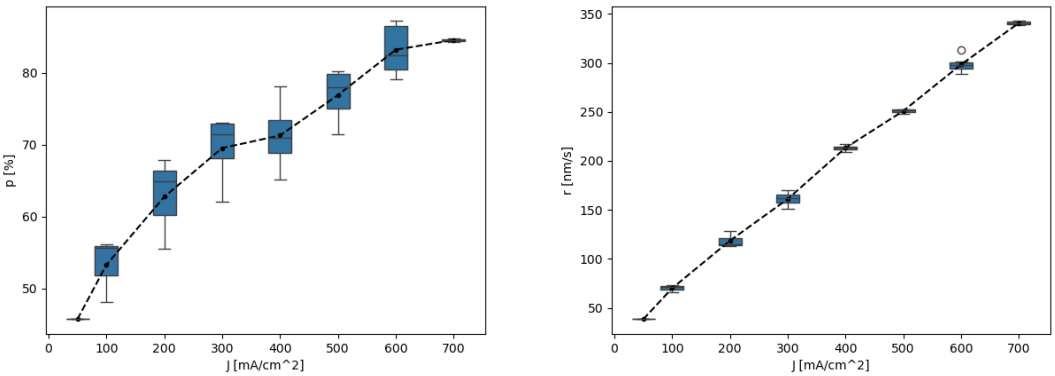

(a) (b)

Figure 3.2: Data used, showing the porosity after etching, and the etch rate (with the corresponding uncertainty) for different current density imposed during the etching process. The data was collected by Clémentine Gevers. These relations change with the substrate and were used in order to find the right current and etching time. The dashed line corresponds to the approximation used to fit the data (linear approximation by segments).

The etch rate also depends on the current. The porosity p and thickness t_i are imposed. Once the current is defined, the etch rate can be found using empirical data, fitted linearly (linear approximation by segments). The time required to etch a single layer dt is defined using the etch rate r : $dt = t_i/r$.

The value of the current was chosen in order to match the values found with our model, in section 2.4. The values can be found in table 3.1.

The porosity of each layer was limited to the interval between 50 and 70 % when the reflector was designed. The lower limit (50 %) was imposed in order to limit the required time for the fabrication of the membrane. The etch rate increases with the porosity so the required time of the process could increase a lot with lower values of the porosity. The higher limit was imposed to ensure the solidity of the membrane. Highly porous silicon ($p \geq 80\%$) tend to be very fragile and would be damaged more easily.

Layer	Current density	Total etching time	Repetition
Bragg layer A	7.84 mA/cm^2	1.09 s	10
Bragg layer B	32.7 mA/cm^2	0.45 s	10
Support layer	7.84 mA/cm^2	1420 s	1

Table 3.1: Current density, etch time applied for each layer type and number of occurrence of these layers are presented here. These values are chosen in order to get the values of porosity and thickness presented in table 2.1 (for the 2 layers of the Bragg reflector), or simply imposed (for the support layer).

A porosity of 50 % and a thickness of 80 μm was imposed for the support layer, in order ensure the stiffness and improve the absorption of light in this layer. For this layer, a current of 21.17 mA was used, during 420 seconds.

For each layer, the etching process was stopped during 2 seconds every 10 second of etching (or when the etching process is finished for this layer), in order to leave time for the hydrogen to diffuse out of the membrane and avoid accumulation of bubbles. This technique was used previously. [13]

Lift-off

In this third step, a larger current is imposed to remove the silicon below the porous structure and detach the porous flake from the substrate. This process was used previously in order to create a free-standing porous flake. [18]

Different current values were tested. A current that is too large might saturate directly the current source, whose output voltage is limited to 20V. On the other hand, an inappropriate value might not produce the desired effect or might damage the sample. An optimal value for this current could not be found. Figure 3.3 show the data the results of different tests that were made with different values of the current. Many samples were damaged during the production. This damage might be due to some unknown parameters, different than the applied current. However, the physical properties of the Bragg layer should not depend on the lift-off and one should get similar optical properties with a different current.

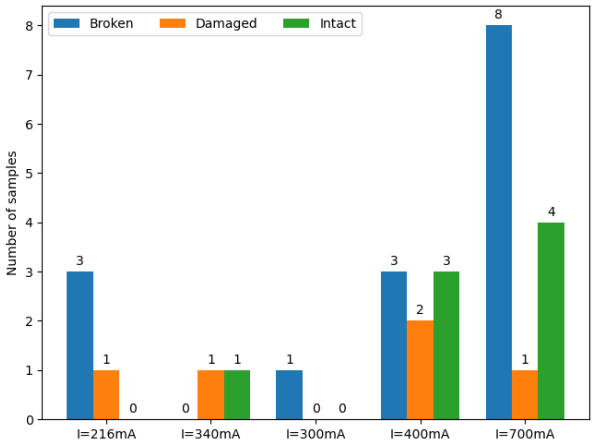

Figure 3.3: Presentation of the number of samples that were produced with different values of the lift-off current. The number of samples that were totally broken, partly broken or undamaged during the production are presented for each value of the current that was tested. The largest value of the current seems more appropriate in order to minimize losses.

The current is imposed during a time δt. The target current is reached rapidly and the impedance increases after some time. The value of δt was chosen such that the voltage saturates before the end of this delay. The minimum values that were used, for different currents I, are the following. Longer delays can be used and should work as well.

- For $I = 216$ or 300 mA: 1 s
- For $I = 340$ or 400 mA: 0.5 s
- For $I = 700$ mA: 0.2 s

The saturation of the voltage indicates that the electrical circuit is opened. This can be explained by an important production of gas (H_2) under the membrane, which is associated with the lift-off process. Figure 3.4 shows the evolution of current and voltage during a typical lift-off process. One can observe the 2 stages of electropolishing and detachment of the flake, corresponding to 2 plateau at a voltage around 10 and 20 V. The voltage of the first plateau can vary depending on the conditions of the experiment. A very large value of the target current should be avoided in order to avoid early saturation before reaching the first plateau. This would make the experiment less reproducible.

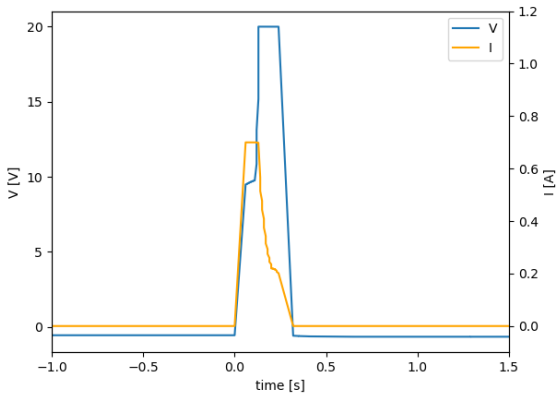

Figure 3.4: Evolution of the applied voltage and current passing in the cell for a target current going from 0 to 700 mA, then back to 0 mA. The voltage stabilizes at a value around 10 V after the target current is imposed at its high value. It then saturates at 20 V until the target current goes back to 0 mA.

3.1.2 Characterization

A scanning electron microscope (SEM) was used to check the nanostructure of the porous silicon. Figure 3.5 shows the cross-section of a flake, produced with the method described previously. The pores, parallel to one another can be observed. The different layers corresponding to the the Bragg reflector can be observed on a more detailed view. The 10 double layers can be identified. The detailed view also shows that the structure is not perfectly regular since the pores can have different shapes and some irregularities appear between the layers of different porosity.

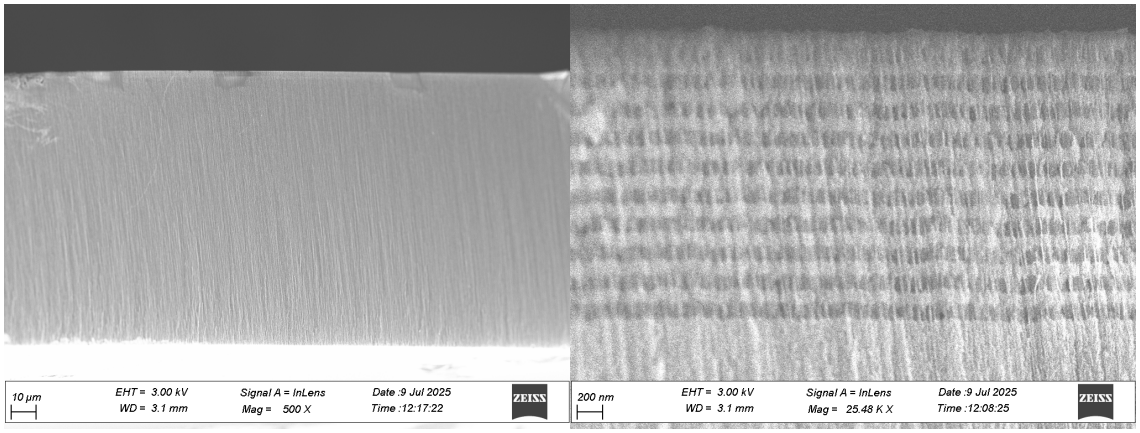

(a) (b)

Figure 3.5: SEM image of a porous silicon flake (a) cross-sectional view representing the whole thickness (b) zoom on the reflecting multilayered stack on top.

Some measurements were made on the 2 images in figure 3.5. The values are reported in table 3.2. These values show that the thickness of the whole flake and of each layer in the Bragg reflector are larger than expected. The etch rate is provided with a given uncertainty and might be larger than the expected value for this sample. The relative error (with respect to our model) we make is quite large (between 10 and 50 %). These measurements are not very significant since the method of characterization, using SEM imaging, is not very accurate. The measured dimensions may appear larger if the cross-section is not perfectly perpendicular to the electron beam. These results only show that the dimensions could be underestimated by a large factor (up to 50 %).

Thickness of	flake [μm]	Bragg stack [μm]	single double-layer [nm]	layer interface (RMS) [nm]
Model	81.4	1.4	140.5	0
Measurements	99.2 ± 8	2.4 ± 0.3	214.6 ± 10.4	43.3 ± 18.1

Table 3.2: Measured values for the thickness of different part of the flake, and comparison with the expected results, computed with our model (see section 2.4)

3.1.3 Oxidation of porous silicon

After the porosification process, the silicon flake is heated in a Heraeus oven. A flow of synthetic air is imposed inside the oven. Silicon reacts with oxygen at the surface of the material, forming SiO_2. The temperature varies in the oven, following these 3 steps:

- The temperature rises from ambient temperature (around 20 °C) to 200 °C during 30 minutes.
- The temperature is kept constant during 30 minutes.
- The temperature slowly decreases. The sample is then taken out of the oven after 50 minutes.

In this process, the silicon near the surface reacts with oxygen and the thickness of oxide layer increases.

3.2 Measuring the reflectance

3.2.1 Setup

A 10 mW halogen lamp was used as a light source. The light beam is guided by an optical fiber. The beam passes through an optical lens and is focused on the surface of the sample. The sample is a silicon flake with a Bragg mirror on the top surface. The flake is placed on a silicon substrate (the same it was extracted from). However, our model predicts that the support below the flake should not change the reflectance spectrum a lot, because the transmittance is low compared to the reflectance.

The reflected beam is collected through the same lens (than used for focusing the beam on the sample) and directed into an optical fiber connected to an Ocean Optics JAZ spectrometer. This spectrometer is controlled by a computer with the OceanView program and a reflectance spectrum in the desired interval of wavelength is computed. The measurement is calibrated in order to reduce the background noise, and the reflected signal is compared to that of the initial beam. The signal of interest is integrated during 250 ms. The integration time was chosen as to maximize the intensity while not saturating the spectrometer. The spectrometer provides an intensity in a unit of counts (cnt), with a single count corresponding to a few tens of photons.

Measurements of reflectance were made previously with a similar setup, on a flake produced with the same technique. [10] In this study (confirmed by our measurements), the measurements were noisy and the samples were attached to the wafer. The samples produced in this case are more difficult to manipulate.

The reduction of the noise is necessary for future analysis. This should help for noise assessment, checking the optical properties of the sample in different situations and for analysis and interpretation of these properties. Different methods were used to help manipulating the samples and improve the signal. These methods are discussed in this section.

3.2.2 Manipulation

The flakes that are produced are small (with a diameter $d \approx 5$ mm), thin, very light and more fragile than bulk silicon. Manipulating these samples can be very challenging. For example, the flakes would be destroyed if they are grabbed directly with a plier. Therefore, some tape was used as a support. It helped for the displacement of the samples after the oxidation, at the end of the production process. An illustration of the sample and the supporting tape is presented in figure 3.6.

This method facilitated handling and reduces the amount of losses. Another advantage is that the membrane can be held and exposed on both sides, and the samples can be placed and measured inside a solution. Therefore, it can then be used as a flow-through membrane. This is an advantage for some applications, in particular for chemical or biosensing. [50][19] However, it does not solves all issues related to the manipulation of the flakes. For example, it did not help for the SEM analysis because the flake does not break neatly (with or without the support) and the flakes could be damaged when placed on the support. This is mostly due to the brittleness of the flake and the issue should stay the same when using a different support material.

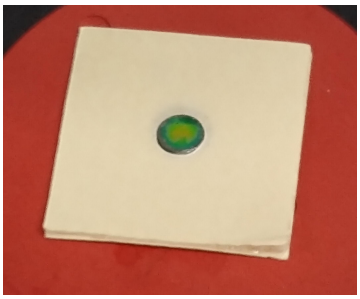

Figure 3.6: Representation of a silicon flake held with a piece of tape. This solution was used for the displacement and ease the measurement of the reflectance on the sample.

3.2.3 Surface scan

Description

Figure 3.7 show that the surface of the flake is inhomogeneous and different colors are visible at the surface. This can be explained by an etching process that is different on the edges and at the center of the porous structure.

Because of the setup, the voltage applied between the platinum electrode and aluminum foil (see section 3.1.1) produces an electric field that is not perfectly homogeneous on the surface of the wafer. Its intensity can be different near the edges and at the center of the flake.

The etch rate and resulting porosity may vary between the edges and center, leading to inhomogeneities in the optical response (the refractive index depending on the porosity).

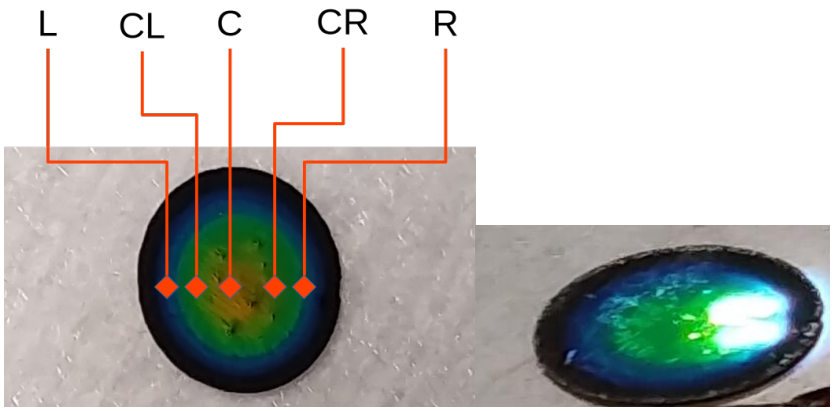

(a) (b)

Figure 3.7: (a) Image of the surface a sample and representation different spots at the surface: on the left (L), center left (CL), center (C), center right (CR) or right (R) of the surface. The color is different at these different spots. (b) Same sample illuminated (near the edge) by the incident beam. The surface illuminated is smaller than the reflecting surface.

However, a more homogeneous structure is expected around the center of the flake. [16] This is shown by the visual appearance and measurements presented on figure 3.8. The measurements of the reflectance taken near the edges of the flake show a blue shift compared to the others. The wavelength at peak reflectance λ_T is very similar for the measurements not taken near the edges.

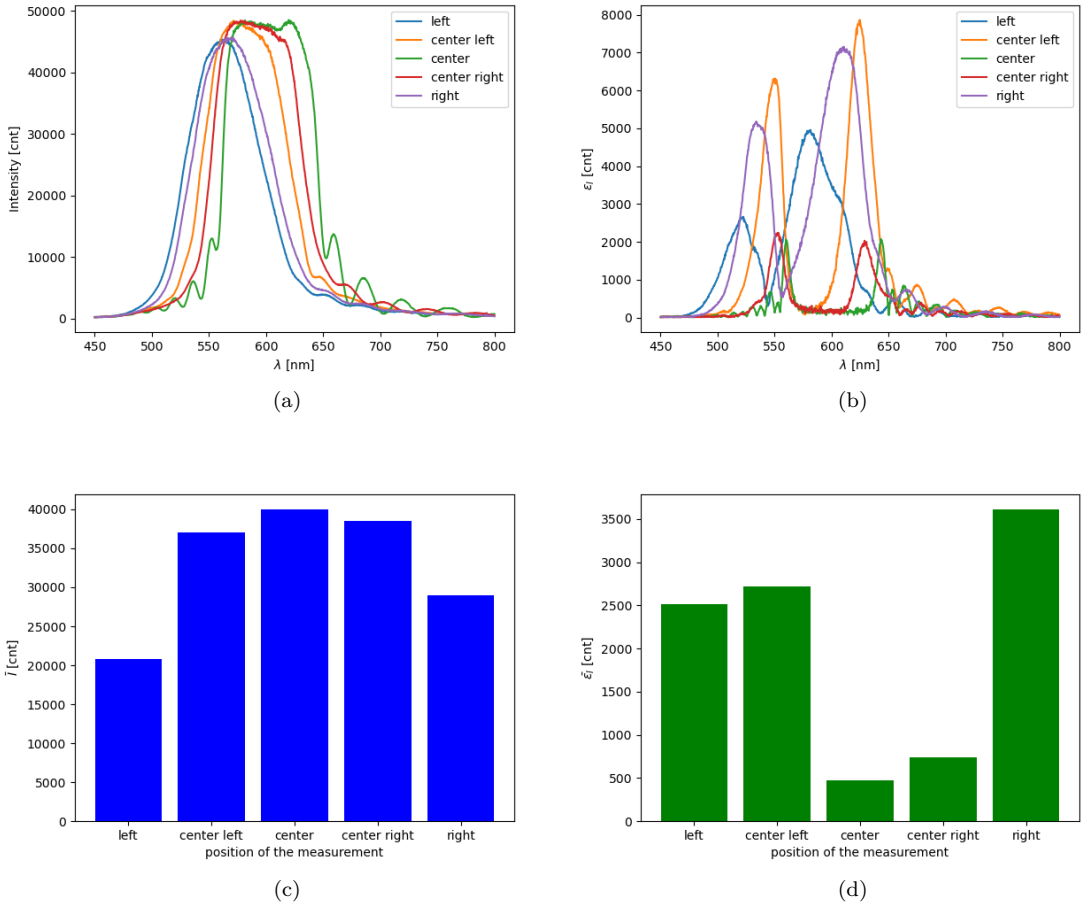

Figure 3.8: The spectra above show (a) the measurement of the reflected intensity when the incident beam illuminates a different part of the sample (represented in figure 3.7) and (b) the standard deviation found for each measurement. The lower graphs show the values of the previous graphs, averaged in the interval of interest, for a wavelength between 550 and 650 nm. The intensity of the peak is lower at the center, and the variance on the measurement is higher near the edges of the sample.

Figure 3.8 also shows that the amplitude of the reflected signal decreases when the beam is reflected on the edges of the sample. This is mostly due to a lower intensity of the incident beam at lower wavelength (this result is show in section 3.2.5). The reflectance measured near the center of the flake show less variations. Therefore, the relative error on the measurement is higher near the edges of the samples for 2 reasons: because of the lower intensity of the signal and because of the geometry of the sample.

Because of these homogeneities, it was decided to only measure the reflectance spectrum around the center of the flake. This should reduce the variations in target wavelength and peak reflectance.

3.2.4 Computing the reflectance

The reflectance spectrum for a single sample corresponds to the ratio of the intensity of the reflected signal and incident beam (from the light source). The intensity of the background noise can also be

measured and used to improve the value of the reflectance. With the intensity measured for the incident beam, reflected beam and background noise denoted respectively as $I_{l(\lambda)}$, $I_{s(\lambda)}$ and $I_{n(\lambda)}$, the computed reflectance has the following expression.

$$R_{(\lambda)} = \frac{I_{s(\lambda)} - I_{n(\lambda)}}{I_{l(\lambda)} - I_{n(\lambda)}} \tag{3.1}$$

However, the intensity of the incident beam is not known and could not be measured directly. It depends on the light source and on the setup. The optical system used to guide and focus the beam generates some losses. A reference sample should be used in order to compute the intensity of the incident beam. Its reflectance should be known for all wavelength in the interval of interest. The intensity of the incident beam can then be computed from the intensity of the beam reflected on the reference sample, that can be measured directly.

The intensity of the light source and of the beam reflected on different reference materials is shown on figure 3.9. The beam reflected on the silicon wafer is not a good reference signal. The intensity is relatively small and mostly depends on the roughness of its surface. This can be explained by the very fast increase of the diffusion of light with the roughness on the surface, that increases exponentially with the roughness squared. [38]

This value is not known at this point. The reflectance of the silicon sample can be computed but would require specific measurements and physical models. A mirror (Avantes RS2 reference tile) was also tested as a reference. Its reflectance should be known approximately. However, the measured signal seems very low. The reflectance of this mirror seems lower than the value in the datasheet. The expected value for the reflectance is around 85 % and depends on the wavelength. [34] But this reflector might be damaged and, compared to other references, the measured reflected signal did not seem to match the expected value of the reflectance, especially for lower wavelength, below 650 nm.

Aluminum foil has also been tested as a reference. Its reflectance depends on its roughness (as for silicon) and can't be known accurately. But the reflectance is expected to be around 80 %, and relatively homogeneous in the interval of interest (when the wavelength is around 600 nm). [31] This is a rough estimation and might induce some errors in our results. But this reflectance will be used as a reference for future measurements. The exact value of the reflectance is not critical for this study so the error seems acceptable.

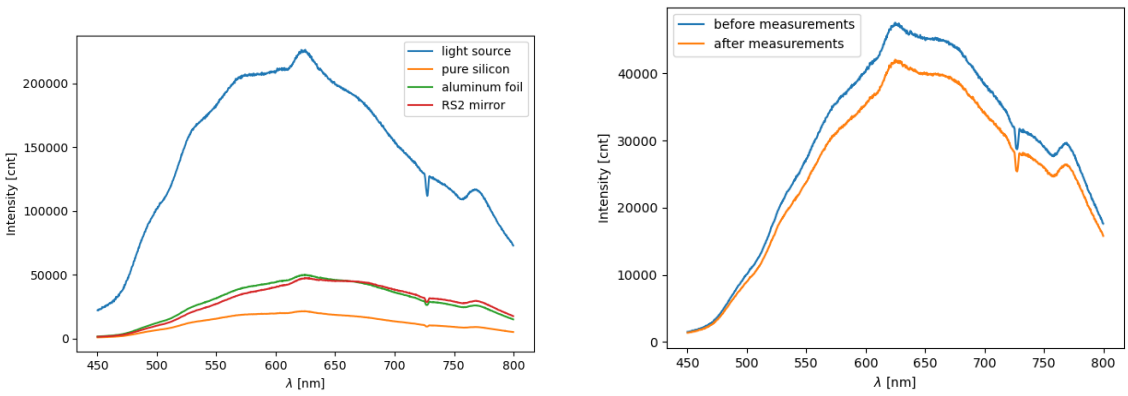

(a) (b)

Figure 3.9: (a) Intensity of the signal, light source and background noise and (b) reflectance spectrum of a sample, calculated with the spectra shown in (a). The peak reflectance, wavelength and width are also represented in (b).

The intensity of the light source is relatively constant between each measurement. However, some variations can be observed over time. Figure 3.9 show that variations between 0 and 20 % can be observed on the intensity of the reference signal, after a delay of a few hours. These variations could be reduced by waiting for the light source to heat up, as it is recommended. [39] These variations could induce some error, but were not taken into consideration at this point.

Once the reference intensity $I_{l(\lambda)}$ is set, one can compute the reflectance with equation 3.1. An illustration of $I_{l(\lambda)}$, $I_{s(\lambda)}$, $I_{n(\lambda)}$ and the corresponding reflectance can be found in figure 3.11.

3.2.5 Noise reduction

Some variations of the amplitude of the reflectance can be observed between different measurements of reflectance taken on the same sample. Different sources could induce such variations: external perturbations, computation errors, defects or impurities at the surface of the wafer, limitations of the setup and instruments, etc.

Several measurements can be used and averaged to reduce the noise. Figure 3.10 shows how the signal changes when several measurements are used to improve the spectrum of intensity. When the mean between N_m different measurement is computed, the variations are reduced and the spectrum is more reproducible. The plot of the variance shows that the standard error decreases with N_m. This is particularly visible for the intensity of the beam reflected on a sample. For a gaussian noise with mean equal to 0, the error is expected to decrease with the square root of N_m. The value $N_m = 5$ will be used in the future.

The reduction of the error in the interval of interest, shown in figure 3.10, does not follow exactly the expected trend (proportional to $1/\sqrt{N_m}$). This can be explained by a relatively high uncertainty on the measurement (confirmed by the results presented in section 3.3). More points (or experimental data) would be required to validate the expected trend.

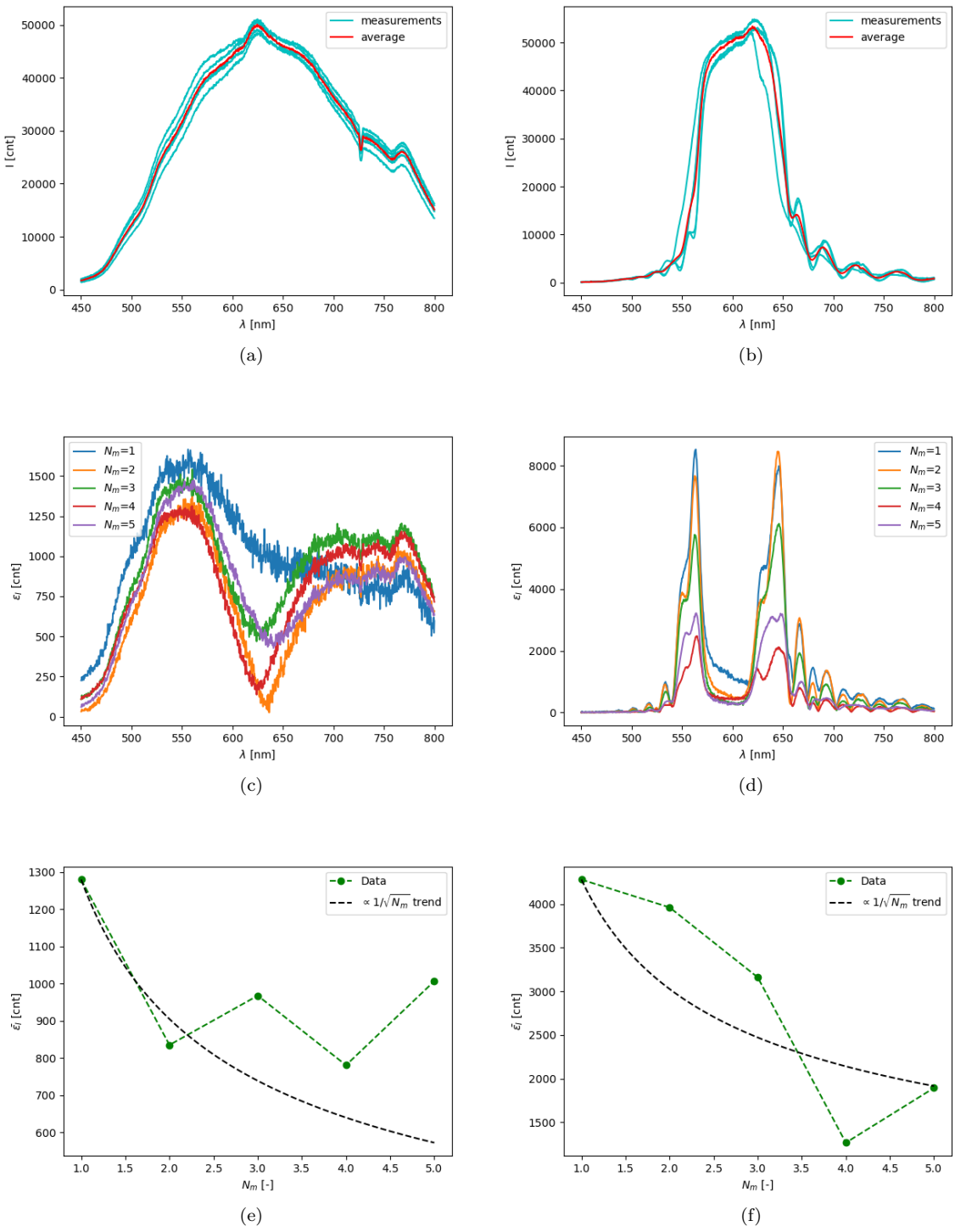

Figure 3.10: On the left (a, c, e), data for the reference signal (incident beam) and on the right (b, d, f), data for the beam reflected on the sample. Top spectra (a, b): intensity of the beam reflected on a sample (5 measurement and the computed average). Middle spectra (c, d): standard error found between different spectra of the intensity at different wavelength. Each spectra is the average of N_m measurements (N_m going from 1 to 5). It shows a decrease of the error with the number N_m. Lower graphs (e, f) show the mean standard error for different values of N_m, in the interval of wavelength that is the most significant: $\lambda \in [550, 650]$ nm. These values are compared to the expected trend, when the noise added to the signal has a gaussian distribution, centered around 0. This confirms the noise reduction in the interval of interest.

In order to improve the precision of the measurement, one should improve the signal-to-noise ratio (SNR), ratio between the average amplitude and the root mean squared (RMS) error. Figure 3.10 also shows that the signal of the light source is lower for low and high values of the wavelength. Therefore, the SNR of the source should be lower at these wavelength, in particular for lower wavelengths. However, the part of the spectrum that is the most interesting in this work is the peak of reflectance, expected to be centered at a wavelength around 633 nm. The SNR should be better in the interval of interest, between 550 and 650 nm.

The intensity of the background noise, reference signal and signal reflected on the sample are first improved by averaging several measurement. The reflectance can then be computed (see section 3.2.4) and the noise has impacts less the results.

3.2.6 Figure of merit

In this study, the most interesting values are found in the reflectance spectrum: the peak reflectance, its corresponding wavelength and the width of the peak.

The peak reflectance R_P correspond to the maximum value of reflectance in the spectrum. The corresponding wavelength λ_P is the wavelength for which the reflectance is $R_{(\lambda_P)} = R_P$. The width of the peak or full width at half maximum $\Delta\lambda$ is the interval of wavelength λ including λ_P where $R_{(\lambda)}$ is larger than $R_P/2$. These values are illustrtated in figure 3.11, along with the 3 signals used to compute the reflectance.

In a very good reflector, the peak has a rectangular shape, and the value of λ_P is hard to compute. The exact value might change a lot with the noise. Therefore, it is important to characterize the peak, not only with λ_P but also with the wavelength at the center of the peak, λ_C. The wavelength λ_C is defined such that $R_{(\lambda)}$ is larger than $\frac{R_{(\lambda_P)}}{2}$ for all wavelength λ in the interval $[\lambda_C - \frac{\Delta\lambda}{2}; \lambda_C + \frac{\Delta\lambda}{2}]$.

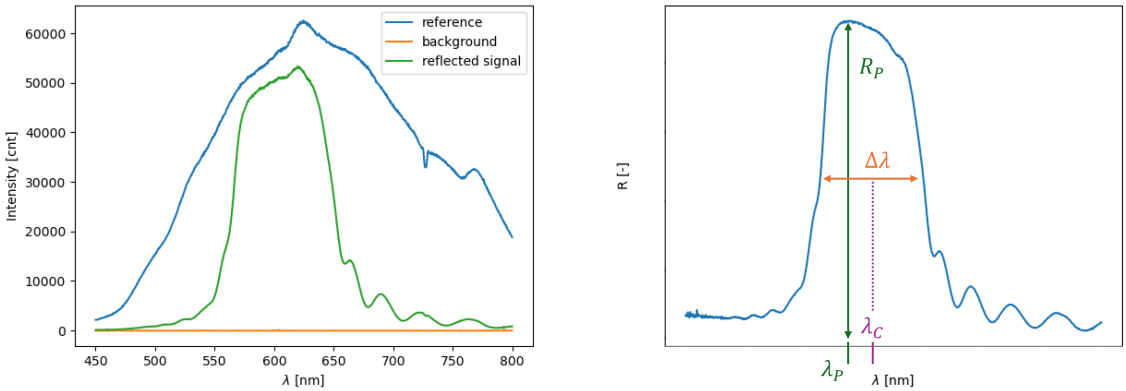

(a) (b)

Figure 3.11: (a) Intensity of the reflected signal, reference signal and background noise and (b) reflectance spectrum of a sample, calculated with the spectra shown in (a). The peak reflectance, wavelength and width are also represented in (b).

In a good reflector, R_P and $\Delta\lambda$ should be maximized, and λ_C should be very close to the target value λ_T.

3.3 Optical measurements and analysis

The optical properties of different samples are meaasured and computed in this section. These properties are compared with the expected results, found with our model.

3.3.1 Values of the model

In this part, 3 different samples are compared. The parameters used for their fabrication are the same and can be found in section 3.1. Their reflectance are compared and the parameters of the reflectance peak are found.

Reflectance spectrum

Figure 3.12 shows the reflectances spectrum of different samples that were tested. The shape, intensity and position of the peak of reflectance are quite different. Multiple measurements were made.

The same figure also show different reflectance found with other measurements and on the same sample. The shape of the peak can change. The values from different measurements can be used to compute the error on the measurement.

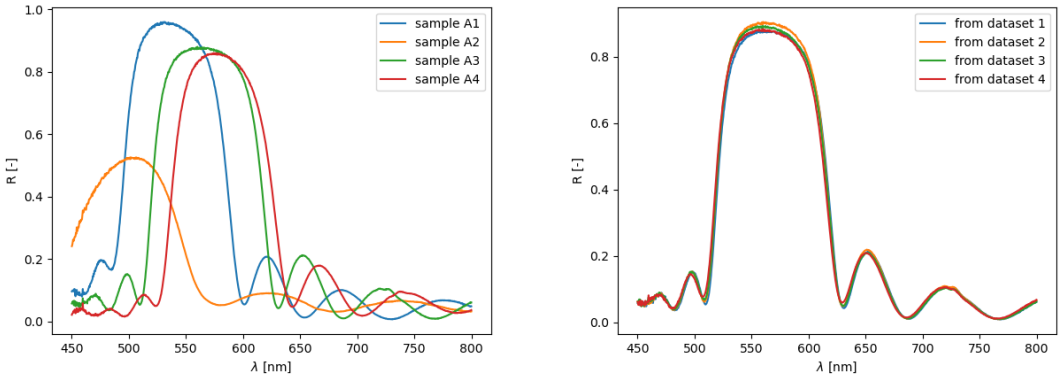

(a) (b)

Figure 3.12: (a) Reflectance spectrum of different samples produced with the same fabrication parameters and (b) reflectance spectra computed with different measurements on the same sample. These graphs illustrate the variations of the optical properties on the measurements (b) and the sample-to-sample variations (a).

Characterization

In the numerical simulations, the maximum reflectance was found at the center of the peak of reflectance. However, the wavelength at the maximum reflectance λ_P does not perfectly match the center of the peak in this case. So, in this case, it is important to consider the center of the peak λ_C in order to characterize the peak.

These values for the characterization of the peak can be found in table 3.3, along with the error on the measurement.

Sample	$R_P[\%]$	$\Delta\lambda[nm]$	$\lambda_P[nm]$	$\lambda_C[nm]$
A1	95.1 ± 0.7	89.6 ± 0.3	531.6 ± 1.8	540.2 ± 0.4
A2	49.7 ± 3.3	93.6 ± 1.8	500.7 ± 1.6	501.1 ± 1.0
A3	89.0 ± 1.0	95.6 ± 0.3	560.0 ± 0.1	567.9 ± 0.7
A4	85.8 ± 1.2	87.7 ± 0.2	574.7 ± 0.6	581.8 ± 0.4

Table 3.3: Characterization of the peak of reflectance of different samples produced with the same process.

Summary

The measurements for the sample A2, shown in table 3.3, show a higher error on the measurement ϵ_m. This can be explained by the lower intensity of the light source (see section 3.2.5).

Besides ϵ_m, another error can explain the variations between our measurements. The samples can be different and some variations can be observed in their properties. This is the statistical error, or sample-to-sample variation, written ϵ_s. The mean standard error ϵ_t can be calculated using both ϵ_m and ϵ_s.

$$\epsilon_t = \sqrt{\epsilon_m^2 + \epsilon_s^2} \tag{3.2}$$

A summary of the experimental results for our samples is presented in table 3.4. The error is more than 5 times larger than in the previous case, and the standard error ϵ_t is almost equal to the statistical error ϵ_s.

$R_P[\%]$	$\Delta\lambda[nm]$	$\lambda_P[nm]$	$\lambda_C[nm]$
79.9 ± 17.8	91.6 ± 3.2	541.8 ± 28.3	547.7 ± 30.8

Table 3.4: Characterization of the peak of reflectance found experimentally.

3.3.2 Thicker reflector

The value found for the reflectance R_P is lower than the expected value, presented in table 4.1. This can be explained by a high transmittance. In that case, increasing the number of layers in the Bragg reflector should increase the value of R_P.

In this section, 6 other samples with a different number of layers are characterized and compared with the previous results. The parameters used for their fabrication are similar to those found in section 3.1, except for the number of layers N. For the Bragg stack, the first samples were made with 20 layers of each type ($N = 20$) and other samples were made with 40 layers of each type ($N = 40$).

Reflectance spectrum

Figure 3.13 shows the reflectance spectra found for these new samples. The lateral shift in wavelength is less visible, but the shape of the peak changes a lot between these samples.

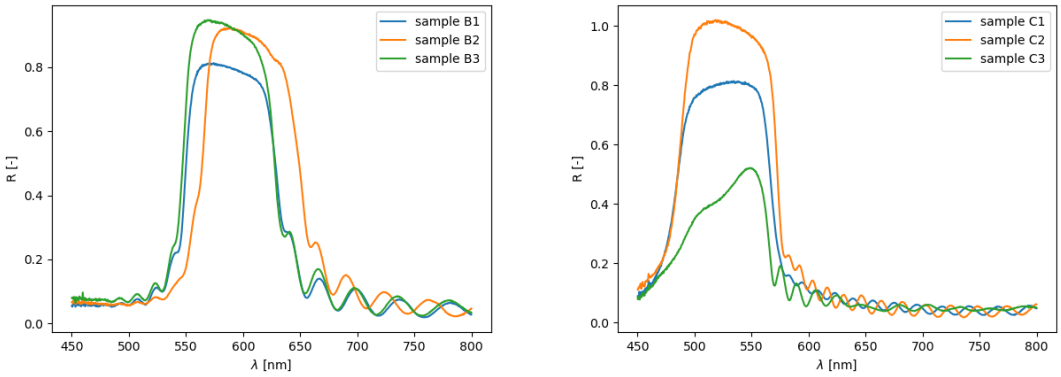

(a) (b)

Figure 3.13: Reflectance spectrum found for different samples for a number of layer (of each type, A or B) in the Bragg stack equal to 20 (a) or 40 (b). Each line corresponds to a different sample. Variations between samples are clearly visible, but the variations in the number of layers is not visible here.

Summary

In this case, the error on the measurement can not always be neglected. Therefore, it is important to also consider the error on the measurement. The characterization of the peak of reflectance for the different types of samples is presented in table 3.5.

N	$R_P[\%]$	$\Delta\lambda[nm]$	$\lambda_P[nm]$	$\lambda_C[nm]$
10	79.9 ± 17.8	91.6 ± 3.2	541.8 ± 28.3	547.7 ± 30.8
20	89.7 ± 6.0	83.9 ± 2.8	576.5 ± 6.3	593.9 ± 7.5
40	79.0 ± 21.1	84.0 ± 4.2	533.1 ± 12.3	526.9 ± 1.8

Table 3.5: Characterization of the peak of reflectance found experimentally with different samples that were made with a number of double layers N equal to 10, 20 or 40.

3.3.3 Different filling media

In this part, a fluid is added to the sample. It infiltrates the pores and changes the optical properties. The measurements are made with different fluids that have different refractive indices. These results can be used to validate the change in the reflectance spectrum. An estimation of the sensitivity can be made. The sensitivity is then used to discuss the use of these samples for sensing applications.

2 different samples were tested: A1 and A4. The peak reflectance was different for these samples. The variations of optical properties of these can then be compared. A similar trend is expected, with a shift of the peak towards larger wavelength (see section 2.5).

Reflectance spectrum

Figure 3.14 shows the reflectance spectra for each sample, each measured with a different filling medium. For a liquid medium with a refractive index higher than air, the amplitude of the peak reflectance decrease and a red-shift is observed. This correspond to the expected result (see section 2.5).

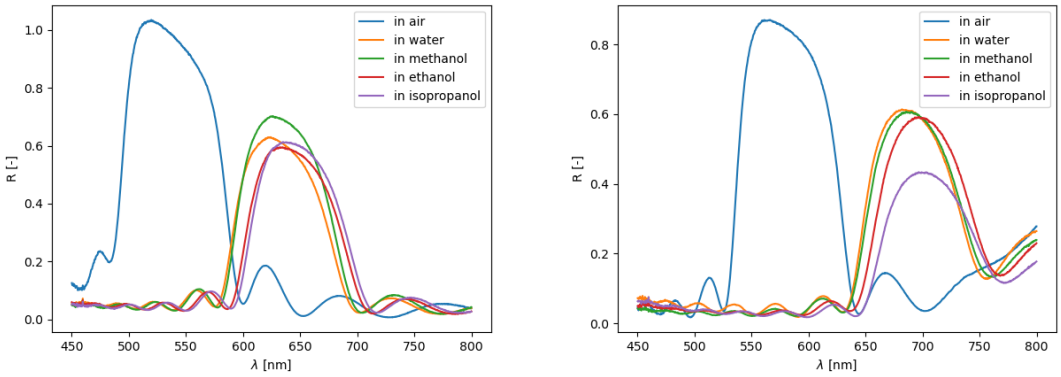

(a) (b)

Figure 3.14: Reflectance spectrum found for different samples for a number of layer (of each type, A or B) in the Bragg stack equal to 20 (a) or 40 (b). Each line correspond to a different sample. Variations between samples are clearly visible, but the variations in the number of layers is not visible here.

Characterization

The figure of merit for each spectrum are presented in tables 3.6 and 3.7. These confirm the observations on the peak reflectance. The shift of the peak is high (larger than 100 nm) compared to the standard error (about 1 nm) and the relative change on $\Delta\lambda$ is quite low (below 10 %).

Medium	$R_P[\%]$	$\Delta\lambda[nm]$	$\lambda_P[nm]$	$\lambda_C[nm]$
air	99.7 ± 4.1	89.0 ± 0.3	521.5 ± 3.5	538.4 ± 0.4
water	63.0 ± 0.6	82.9 ± 0.2	623.6 ± 1.0	633.3 ± 0.3
methanol	66.1 ± 2.4	83.0 ± 0.4	625.6 ± 0.6	635.8 ± 0.3
ethanol	61.4 ± 1.8	83.6 ± 0.0	634.1 ± 0.7	644.4 ± 0.4
isopropanol	59.9 ± 1.0	83.2 ± 0.1	636.4 ± 0.9	648.0 ± 0.2

Table 3.6: Characterization of the peak of reflectance for the sample A1. For each entry, the pores of the samples were filled with a different liquid.

Medium	$R_P[\%]$	$\Delta\lambda[nm]$	$\lambda_P[nm]$	$\lambda_C[nm]$
air	87.1 ± 0.1	87.7 ± 0.7	565.1 ± 2.1	580.8 ± 1.1
water	60.5 ± 0.5	85.5 ± 0.3	682.6 ± 1.5	692.3 ± 1.0
methanol	56.0 ± 2.8	86.0 ± 0.4	684.0 ± 1.1	693.1 ± 0.6
ethanol	59.6 ± 0.6	86.1 ± 0.4	696.5 ± 0.5	702.9 ± 0.6
isopropanol	43.6 ± 0.2	86.9 ± 0.3	700.6 ± 2.9	706.8 ± 0.3

Table 3.7: Characterization of the peak of reflectance for the sample A4. For each entry, the pores of the samples were filled with a different liquid.

Chapter 4

Discussion

4.1 Comparison with the model

4.1.1 Numerical model

The expected reflectance spectrum can be computed using the transfer matrix method (see section 2.2). It is illustrated in figure 4.1. The target wavelength is $\lambda_T = 633$ nm and the peak of reflectance is expected to be centered around this wavelength. The maximum reflectance should be high and the peak width should be around 100 nm (see table 4.1).

The figure also shows that the transmittance in the model is low (lower than 1.5 %). So most photons are reflected or absorbed in the sample. Therefore, the material present below the sample should not change significantly the measurement of the reflectance.

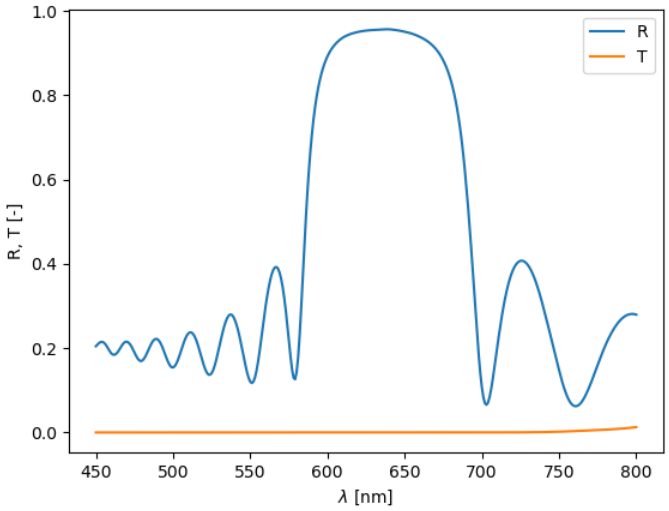

Figure 4.1: Illustration of the reflectance and transmittance spectrum of a PSi flake, computed with the transfer matrix model. The geometrical parameters are presented in section 2. The transmittance is lower than 1.5 % for all wavelengths.

$R_P[\%]$	$\Delta\lambda[nm]$	$\lambda_P[nm]$	$\lambda_C[nm]$
95.7	106.8	638.9	638.9

Table 4.1: Expected result, using the method described in section 2.

This reflectance spectrum found using TMM is oscillating, with a large peak of reflectance around a wavelength λ_P. These are expected for a Bragg reflector. The fringes and peak of reflectance are also present in the measurements. This validates the production of a Bragg reflector.

However, the measurements shown in figure 3.12 show some differences in the reflectance spectrum. The position of the peak, and its shape are different than expected. Our model also does not explain the differences between individual samples Different factors can change the reflectance. These are discussed in this chapter.

4.1.2 Limitations of the design

The results shown in table 4.1 do not match the expected values found during the design step: a target wavelength $\lambda_T = 633$ nm and a maximum reflectance $R_T = 95.7\%$. A first explanation is that a simpler model was used to estimate the optimal design parameters: porosity and thickness of the layers, number of layers. Values were rounded and the presence of the support layer was neglected. But this does not change the values of reflectance.

With a comparison with the more precise TMM model, similar differences were found between the model and the experiments. Therefore, the optical model used as a reference does not model properly the sample. The limitations of the model may have different origins: either it does not describe correctly the physical phenomena occurring in the sample (reflectance, absorbance, and transmittance), or the parameters of the reflector (geometry, refractive index of each layer) were not estimated properly. These limitations are discussed in the following sections.

4.1.3 Absorbance and transmittance

The penetration depth d_p of a light source in a material is defined as the depth at which the beam intensity falls below $1/e \approx 37\%$ of its initial value. This depth can be computed with the attenuation coefficient:

$$d_p = 1/\alpha \tag{4.1}$$

At the target wavelength (633 nm), d_p has a value around 5.6 μm when the porosity is $p = 50\%$. It increases with the porosity. This value is much larger than the thickness of the Bragg stack, that is expected to be 1.4 μm.

The reflection of the beam were described with the Fresnel equations (see section 2.2). If the power of the reflected beam is lower than expected and the power of the transmitted beam is higher, then the reflectance will be lower. In that case, increasing the thickness of the Bragg stack should increase significantly the reflectance R_P.

The model predicts a small increase of the reflectance with the number of double layers N. However, the experiments made on samples with larger values of N show no significant increase in the value of R_P. The small variations come from the error (the standard error goes up to 27 % of the mean value). Therefore, the Bragg stack does not have a high transmittance and the power that is not reflected must be absorbed or diffused.

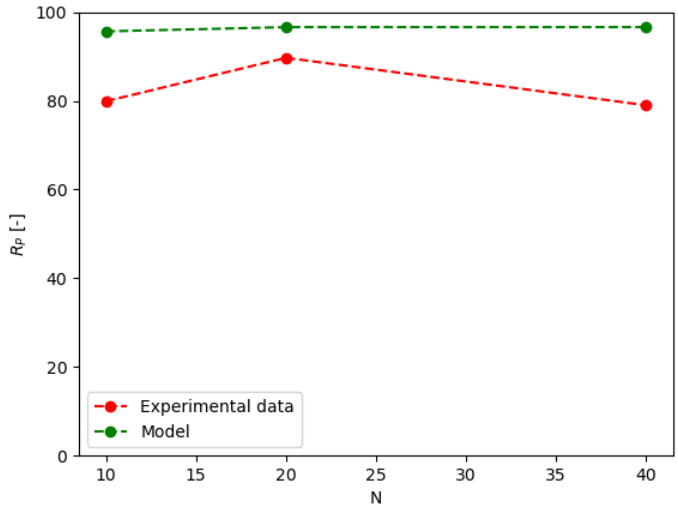

Figure 4.2: Comparison between the maximum reflectance in the experimental data (average value) in the numerical model.

The absorption of light inside PSi can be calculated with the attenuation coefficient. With the different methods from section 2.2 used to compute the power absorbed in the Bragg stack, the losses are small and the reflected power R_P is close to 100 %. So one would expect that the incident light would diffuse inside the Bragg structure. As a consequence, the reflected beam is then not focused and the reflected power R_P is reduced.

4.1.4 Interfaces

Scattering

Figure 3.5 shows some rough edges at the interface between 2 layers in the Bragg stack. When a photon reaches an interface, it can be reflected. With a very smooth interface, the reflection is specular. The numerical model can be used to predict the reflected power P_0, which depends on the wavelength. With an RMS roughness $\sigma > 0$ at the interface, the reflection is diffuse. The power reflected perpendicular to the surface has the following expression. [32]

$$P = P_0 \exp\left(-4(2\pi n\sigma/\lambda)^2\right) \tag{4.2}$$

In the expression of the reflected power, n is the refractive index of the first or the second layer at the interface, depending on the polarization of the light beam (light is not polarized in the experiments).

The roughness can be estimated with the images from the SEM. A value of 43 nm (with a large uncertainty) was found (see table 3.2). A different experiment (with another type of wafer and solvent) produced samples with a roughness in the same order of magnitude (around 30 nm). [38] With $\sigma = 43$ nm, half of the reflected power is diffuse: $P/P_0 = 48\%$.

If the roughness is different between each sample, this model could explain the different amplitudes of the peak reflectance. It was also shown that the roughness changes with the porosity. Producing the samples at a lower temperature can reduce the roughness at the interface. [38]

The model presented here only consider a single reflection of the incident beam. If the value of σ is known, a more complex and more accurate numeric model can be used to compute the reflectance. It should consider multiple reflections, and the impact of the diffusion, that decreases the transmitted power (perpendicular to the surface) at each interface. A TMM model taking into account the roughness was not used for this work and is not necessary to prove that the roughness decreases significantly the reflected power.

Modelling the transitions

When the diffusion of light is neglected, the rough edges induce a change of the porosity at the interface between the layers. For the numeric model, the assumption was made that the interface between layers has a negligible thickness, and that the porosity is homogeneous in each layer. A better model should take into account a region at each interface where the porosity is different than the values imposed in the 2 surrounding layers.

Figure 4.3 shows a numerical simulation, where intermediate layers are added at the interfaces inside the Bragg reflector. The thickness of these layers (centered at the interface is imposed, and the porosity is the average of the values for the previous and next layers. This figure shows that the change in porosity at the interface can reduce the amplitude of the peak. The change on the amplitude is smaller than that induced by the diffusion of light and it can not be the main cause of the change in amplitude compared to the model.

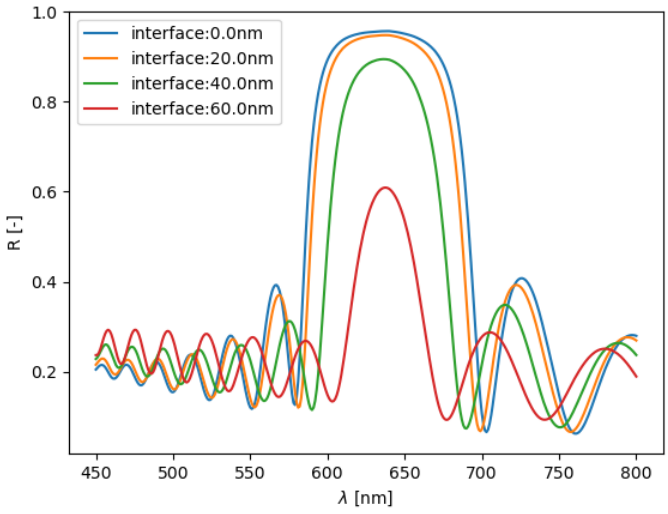

Figure 4.3: Comparison between the maximum reflectance in the experimental data (average value) in the numerical model.

Shape of the peak of reflectance

The shape of the peak of reflectance is also different compared to the model. Different shapes were observed in the results: a round peak, or a peak that has a flat edge on the top. This edge can have a positive or negative slope. The shape can be described by the the difference of wavelength $\lambda_P - \lambda_C$, that can be positive, negative or close to 0.

These changes are not explained with the simulations. However, light scattering depends on the wavelenght. Therefore, it could change the shape of the reflectance spectrum. Further analysis would be required to check the impact of the interfaces on the shape of the spectrum.

4.1.5 Etching process

The current source used for the etching process has a good precision (about 100 nA) and slope for the transient phase of 0.6 μs/V. Its maximum reading frequency (with the setup used here) is 1600 readings/s. [42] It was observed experimentally that, when a new target current is imposed, the transitions time is around 60 ms and the current is met with an error below 0.1 %. At this point, the slope of the current is expected to be similar when the target current is high or when it is low. In a controlled environment, the production method should be reproducible, with a low error on the geometry, porosity and reflectance. But the porosity and etch rate also depends on the temperature and concentration (and type) of the solvent. The doping level of the substrate also impacts the etching process, and no measurements were performed to verify the substrate homogeneity. All these perturbations can change the resulting porosity and thickness of the layers in the samples.

Figure 3.2 shows the uncertainty on the values of porosity (p) and etch rate (r). The uncertainty on r is also the error on the thickness of the layers. The relative value for the standard deviation σ is around 4.5 % for p and 5 % for r.

Figure 4.4 show a simulation, when a constant relative error is imposed on the thickness or porosity of each layer in the Bragg stack. At a distance σ from the optimal value, the geometry and porosity do not change a lot the value of R_P (relative error around 0.5 %). But a significant change (a relative error around 5 %) is observed $\Delta\lambda$ and the position of the peak (λ_P or λ_C).

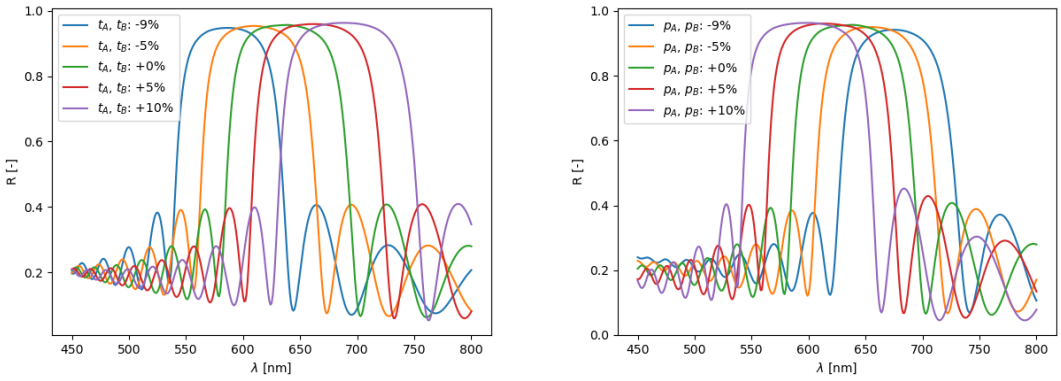

(a) (b)

Figure 4.4: Simulation of the reflectance spectrum computed using TMM, and adding a constant error on (a) the thickness or (b) the porosity of all layers in the Bragg stack. The error is a fraction of the optimal value.

These results predict a variable shift of the peak reflectance. But a systematic blue shift was observed experimentally. The simulations presented here do not explain the blue shift. Also, the error on the position of the peak found experimentally (see table 3.4) was too large and does not match the standard deviation found for the porosity and etch rate.

The results from SEM measurements (see table 3.2) show that a large systematic error the dimensions is possible, but the dimensions should be larger, inducing a red-shift on the peak. Given the results of the measurements, only a large systematic error on the porosity could explain the blue-shift. The exact origin of this error is unknown, but different possible causes are identified:

- An error during the characterization of the wafer or area exposed to the etch solution (choice of the current).
- An inconsistency during the manipulation, and in particular during the porosification of the sample.
- An environmental factor or fabrication parameter that was not identified and that influence the optical properties.

The characterization of the wafer was made considering a different area exposed during the etching process. That makes the computations of the current and time delays less reliable. Also, the impact of each fabrication parameter could not be assessed. For example, it is expected that the lift-off does not change the optical properties, but this could not be proven experimentally because of the issues faced with the fabrication (see section 3.1.1). In the end, the exact cause of the blue-shift can not be proven with the current results.

4.1.6 Oxidation step

The simulation predicts a peak reflectance for a wavelength around between 640 nm. All samples have shown a blue shift (towards lower wavelength) compared to the model. Another possible explanation for this blue shift is to consider an EOT for each layer that is lower than expected.

It was shown that, for the same geometry, the target wavelength is proportional to the refractive index (see equation 2.16). It was also shown in figure 2.3 that the refractive index of silicon oxide very low, compared to that of pure silicon. Therefore, the refractive index of the porous structure is expected to decrease after oxidation, inducing a blue-shift in the reflectance spectrum.

When the sample is heated in an oven, a fraction of the silicon, reacts with oxygen to form SiO_2. The volume relative fraction of silicon involved in the reaction is written s. The surface exposed to air and the amount of silicon change with the porosity of silicon. So s is expected to changes with the porosity $p = p_{in}$. In this part, we assume that the oxidation degree s is constant.

The reaction of silicon with oxygen increases its molar volume by a factor 2.27, and is associated with a decrease of the porosity. The new porosity is written $p_{ox} = p_{in} - 1.27(1 - p_{in})s$. The volume fraction of $SiO2$ after oxidation is written v_{SiO_2}. The oxidation degree can then be written $s = \frac{v_{SiO_2}}{2.27(1-p_{in})}$. The change in volume must be taken into account to compute the new refractive index. It also imposes a maximum value for s: $s \leq \frac{p_{in}}{1.27(1-p_{in})}$. [2] The Bragg stack in our model has a minimum value for of 50% for p_{in}, and the limit is then $s \leq 78.7\%$.

Figure 4.5 show the refractive indices computed (with a different model than LLL) for different values of s and p_{in}. The figure also shows the reflectance spectrum computed with the numerical model, and for different values of s. A blue shift is visible, and the peak reflectance can shift by 145 nm when the oxidation degree is large.

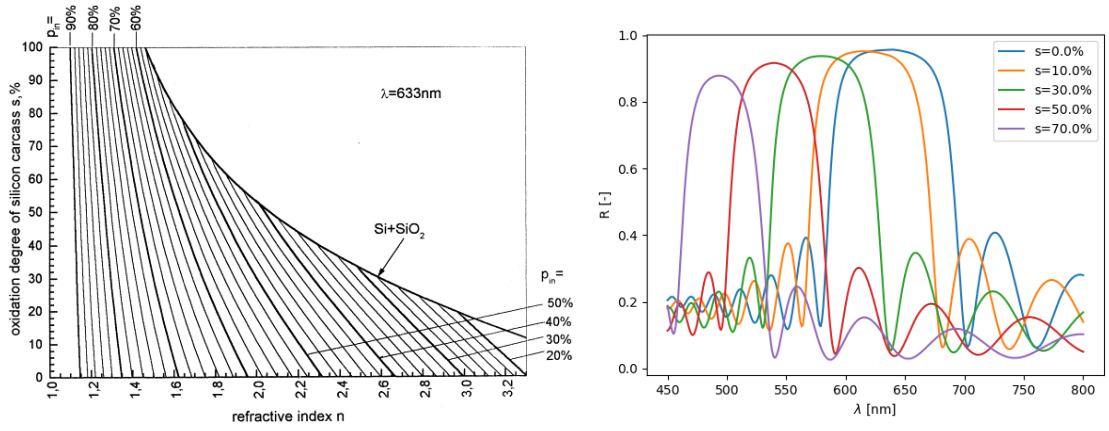

(a) (b)

Figure 4.5: (a) Value of the refractive index of PSi, for different initial porosity and oxidation degree, computed with the Bruggeman's model. [2] (b) Reflectance spectrum, simulated with TMM, and using LLL method to compute the refractive indices.

After being kept at 200 °C for less than an hour, the oxidation degree should be less than 0.1. [28] Therefore, λ_C shifts by less than 20 nm, $\Delta\lambda$ changes by less than 5 %. The impact of the oxidation on the peak value R_P is also negligible (reduced by less than 0.5 % in the model). This confirms that neglecting the oxidation in the model is a good approximation.

4.2 Discussion on the methodology

4.2.1 Sensing

Once a sample has been produced, its optical properties can be assessed by measuring the reflectance spectrum in air. These properties can change when the membrane is placed in a different medium. This change, when it is significantly larger than the error, can be used for sensing the environment. Therefore, the variations in optical properties that were measured are analyzed here.

A change in the refractive index of the filling medium also changes all figures of merit. However, previous results in this chapter have shown that these values changes with different parameters. When the membrane is placed in a solution, the EOT of each layer changes, inducing a shift of the reflectance peak. Other physical phenomena also change the reflectance: the absorption of light inside the reflector, the diffusion at the interfaces and the transmission and reflection at each interfaces also change. Because of these changes, the value of R_P and $\Delta\lambda$ are less reliable and will not be used to compute the sensitivity. The value of λ_P was interesting to discuss the shape of the peak of reflectance, but the change of shape could not be interpreted with the numerical model. Therefore, only the change on λ_C is considered to compute the response of the reflector in different solutions.

The refractive index of each fluid depends on the wavelength. But in this case, only the real part at a wavelength of 650 nm is considered. The refractive index (written n_f) is assumed to be constant for all wavelength. This is a strong assumption, but it should not change a lot the shift of the peak in the model since the EOT depends on the refractive index (real part), the refractive index of air does not change significantly with the wavelength and the position of the peak λ_C is between 630 and 710 nm in the other media. The values of n_f for different fluids are presented in table 4.2.

Medium	n_f [-]
air	1
water	1.331
methanol	1.325
ethanol	1.36
isopropanol	1.375

Table 4.2: Refractive index at a wavelength of 650 nm for different materials. [30]

The presence of a fluid different than air is expected to increase the refractive index of the PSi and, because of equation 2.16, increase the value of λ_C. The sensitivity is defined as the ratio between the change in the position of the peak and the change in refractive index n_f.

$$S = \frac{\Delta\lambda_C}{\Delta n_f} \tag{4.3}$$

Figure 4.6 shows the wavelength λ_C for 2 membranes in different media. These values are compared to the model, computed using the values from table 4.2. The first sample (A1) has a sensitivity around 293 nm and the second (A4) one has a sensitivity around 339 nm. The sensitivity is very different between these 2 models, and these values of very different than the trend found with the model. However, the sensitivity is expected to change with the porosity and it was already stated that the porosity might be very different in the samples compared to the model.

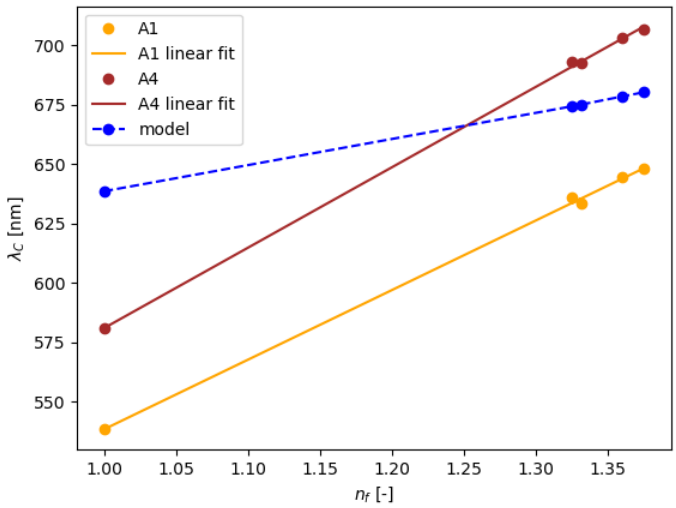

Figure 4.6: Representation of the shift of the peak reflectance in the experimental data for 2 different samples (A1 and A4) in different media. These values are drawn with respect to their refractive index shown in table 4.2. These relations are fitted linearly and compared to the numerical model.

The uncertainty on the position of the peak round in tables 3.6 and 3.7 is around 0.5 nm. The standard error seems random and uncorrelated with the amplitude of the peak. Its main cause could be the limitations of the setup. The data represented in figure 4.6 show that the experimental data do not match the linear fit. The standard deviation compared to the model is around 1.25 nm. Using these 2 errors, one can compute the mean standard error $\epsilon_t = 1.35$ nm.

With ϵ_t and the sensitivity, one can compute the detection limit, defined as the change in refractive index that induces a response (change in λ_C) that is 3 times the standard error. The detection limit is $\delta n \approx 0.013$ in this case and around $5 * 10^{-3}$ with a more precise model (no linear approximation) of the response of the sample. A value in the order of 10^{-3} was expected in the second case. [10] Different devices have a much greater precision, [51] but some improvements in the fabrication, measurement setup or in the model should help to lower the detection limit. Also, the reference wavelength used in table 4.2 might have to be adjusted for each sample in order to lower the error and the detection limit.

In these experiments, the sample-to-sample variation on λ_C and on the sensitivity can be very large. For instance, table 3.4 shows a standard error the order of magnitude of 30 nm. Therefore, a calibration would be required before using these samples for sensing applications.

4.2.2 Experimental challenges

The steps followed for the production and characterization of the samples are the following.

- Preparation of the wafer
- Etching
- Oxidation
- Mounting on a support
- Setting a reference for measuring the reflectance
- Measurement of the reflected beam
- Data analysis

Some steps were challenging, or need to be adapted in order to improve the results.

There is still a lot of uncertainty on the etching process. The porosity can not be chosen with precision. This process also induces some rough edges at the interfaces between the different layer.

Other issues were faced during the etching process. A lot of samples were lost after the lift-off. A better understanding of the process would reduce the amount of samples lost. However, in this case, only 25-50 % of the samples could be used and, for half of the samples, the target wavelength would be outside of the peak of reflectance. For the production of samples with a reflectance higher than $R_P/2$ at the target wavelength, about 80 % of the samples in total would be lost. This induces a greater cost, and more material and chemical wastes would be produced during the fabrication. The financial and environmental impact would be significant. More investigations on the process would be required to improve the production yield.

In these developments, we assumed that the oxidation does not change the dimensions of the layers inside the reflector, and that the change in porosity could be computed with a simple model. However, these hypothesis have not been demonstrated experimentally and might induce some errors in the measurements.

Manipulating the samples was also very challenging. Fastening the samples to some tape can induces some stresses in the structure. Moreover, the samples could not be perfectly flattened before an optical measurement. This increases the uncertainty on the results.

Another great challenge related to the measurements setup was to compute the spectrum of the intensity of the incident beam. The reference that was used to compute this value was very approximative. This also added some uncertainty on the results.

Finally, large differences were observed between the model and the experiments. In another research study using a PSi Bragg mirror, the parameters (porosity, geometry) were first fitted with the reflectance spectrum in air. [45] This method could be used to reduce the error.

4.2.3 Improving the procedure

The precision of the fabrication process could be improved and the interfaces could be smoother by adapting the etching process. The solvent in the etch solution could be changed. A lower temperature also helps reducing the roughness at the interfaces. [38]

For the manipulation of the samples, these should stay on the silicon substrate or be deposited on a surface that matches the shape of the sample. The lower part of the sample is not flat and the flatness of the top surface could be harder to achieve with a different solution.

Also, a reference sample with a reflectance that is known with a relatively good precision should be used to compute the intensity of the incident beam, before measuring the reflectance. Validating its reflectance spectrum might require further developments.

Finally, we recall that making a measurement at the center of the sample and averaging the values of different measurement should each reduced the error approximately by a factor 2. It was also shown that a first calibration of a sample reduced the error by a factor 50. These are encouraging results, making a measurement of the refractive index of a medium possible, with a precision in the order of 1 %, and with some perspectives to increase the precision.

Chapter 5

Conclusion and perspectives

In this work, we first have introduced the subject of PSi reflective Bragg membranes. These reflectors do not stand out because of a high reflectance or reliability, but because of their low cost, porous structure and tunability. The reflective membranes are particularly suitable for sensing a change in the optical properties of the environment.

A physical model was then presented. The modelization of the sample is divided in X steps:

- A mixing rule is used to compute the refractive index of PSi for different values of the porosity, or the porosity for a given refractive index.
- An analytic model, inspired by the TMM, is used to estimated the values of the optimal thicknesses and refractive index of each layer in the Bragg stack.
- A transfer matrix model is used to compute the reflectance spectrum of the reflecting flake.
- The reflectance change with the medium present in the pores. A relation between the reflectance and the type of medium in the structure can be calculated.

The procedure for the fabrication, including the etching in a solution of HF, and the procedure for the measurement were presented. The main issues that were faced with the production in cleanroom were the error on the porosity and geometry, and the reproducibility. Different techniques were proposed to reduce the noise on the measurements. The manipulation of the samples and the measurement of incident beam were the main challenges for the optical measurements. Different samples were made with the same geometry, or with a different thickness of the Bragg multilayered stack. These could be used to get a measurement considering the error on the measurement and sample-to-sample variations. Optical measurements were also made in different solutions, in order to check the compare the sensitivity of these samples with the values of the model.

Finally, a discussion of these measurement and a comparison with the expected values were presented. The peak reflectance was lower than the value of the model and large variations were found in the experimental data. Increasing the number of layers in the reflecting stack did not improve the reflectance significantly. The most likely explanation for the low reflectance is light scattering at each interface. A blue-shift was also observed, and might be explained by a higher porosity in the Bragg stack. The variable porosity at each interface, impact of oxidation and error on the dimensions were also investigated. The measurements in different media showed a low precision compared to other devices. But the some similarities with the model and the linearity of the reflector are encouraging. Some ideas were proposed or recalled to improve the procedure or increase the precision.

Some improvements on the setup that was used here are possible (see section 4.2). More research on the chemical and physical processes involved in the production and measurements of the samples would help to improve the results. A better numerical model could be developed. For example, a model taking into account the roughness. The simulations made with this model would help to analyse the results.

Besides the improvements on the setup and fabrication, the PSi membranes presented here might not be the optimal structure for sensing applications. Different types of samples could be more precise or more reliable.

Introducing a microcavity inside the reflector created a sharp peak in the reflectance spectrum, where the reflectance is lower. The corresponding wavelength could serve as a better reference signal,. An increase in the sensitivity is expected. Previous results have not shown a significant improvement for these membranes by introducing a microcavity. [45] That might be caused by some damage inside the flake. Further research would be required to understand these results.

This study could also be completed by applying another material with a low absorbance inside the porous structure, in order to improve the performance of the membrane. This step would passivate the inner surface of the material and oxidation step would not be required. The deposition of the material and changes in the model would add some challenge. But this other material could also help improve the peak reflectance.

Finally, the potential applications of the samples presented here and the constraints associated to the applications were not discussed in detail in this work. Future research would be required to identify the market, added value and remaining challenges for the usage of this technology in a sensing device.

Bibliography

[1] "Impact of surface charge density modulation on ion transport in heterogeneous nanochannels". Amin Alinezhad, Mahdi Khatibi, and Seyed Nezameddin Ashrafizadeh.
In: *Scientific Reports* 14.1 (2024). ISSN: 2045-2322. DOI: 10.1038/s41598-024-69335-1.
URL: https://doi.org/10.1038/s41598-024-69335-1.

[2] "Effective refractive index and composition of oxidized porous silicon films".
E.V. Astrova and V.A. Tolmachev.
In: *Materials Science and Engineering B* 69-70 (Jan. 2000), pp. 142–148.
DOI: 10.1016/s0921-5107(99)00236-6.
URL: https://www.sciencedirect.com/science/article/pii/S0921510799002366.

[3] "Enhancing the performance of porous silicon biosensors: the interplay of nanostructure design and microfluidic integration". Kayan Awawdeh et al.
In: *Microsystems & Nanoengineering* 10.1 (July 2024). DOI: 10.1038/s41378-024-00738-w.
URL: https://www.nature.com/articles/s41378-024-00738-w.

[4] "Stability of visible luminescence from porous silicon".
J. L. Batstone, M. A. Tischler, and R. T. Collins.
In: *Applied Physics Letters* 62.21 (May 1993), pp. 2667–2669. DOI: 10.1063/1.109279.
URL: https://doi.org/10.1063/1.109279.

[5] "Effective permittivity of porous media: a critical analysis of the complex refractive index model". Alessandro Brovelli and Giorgio Cassiani.
In: *Geophysical Prospecting* 56.5 (July 2008), pp. 715–727.
DOI: 10.1111/j.1365-2478.2008.00724.x.
URL: https://doi.org/10.1111/j.1365-2478.2008.00724.x.

[6] "Berechnung verschiedener physikalischer Konstanten von heterogenen Substanzen. I. Dielektrizitätskonstanten und Leitfähigkeiten der Mischkörper aus isotropen Substanzen".
D. A. G. Bruggeman. In: *Annalen der Physik* 416.7 (Jan. 1935), pp. 636–664.
DOI: 10.1002/andp.19354160705. URL: https://doi.org/10.1002/andp.19354160705.

[7] "Multilayer optical calculations". Steven J. Byrnes. In: *arXiv (Cornell University)* (Mar. 2016).
DOI: 10.48550/arXiv.1603.02720. URL: https://arxiv.org/abs/1603.02720.

[8] "A micro gas preconcentrator with improved performance for pollution monitoring and explosives detection". E.H.M. Camara et al.
In: *Analytica Chimica Acta* 688.2 (2011), pp. 175–182. ISSN: 0003-2670.
DOI: https://doi.org/10.1016/j.aca.2010.12.039.
URL: https://www.sciencedirect.com/science/article/pii/S0003267011000626.

[9] "Iontronics". Honggu Chun and Taek Dong Chung.
In: *Annual Review of Analytical Chemistry* 8.Volume 8, 2015 (2015), pp. 441–462.
ISSN: 1936-1335. DOI: https://doi.org/10.1146/annurev-anchem-071114-040202.
URL: https://www.annualreviews.org/content/journals/10.1146/annurev-anchem-071114-040202.

[10] *Optimisation of a biosensor based on a porous silicon surface for indirect optical detection of bacteria through their lysate*. Elia Colomer Clavel. June 2024.
URL: https://riunet.upv.es/handle/10251/20753.

[11] "Passivated porous silicon membranes and their application to optical biosensing".
Clara Whyte Ferreira, Roselien Vercauteren, and Laurent Francis.
In: *Micromachines* 13.1 (Dec. 2021), p. 10. DOI: 10.3390/mi13010010.
URL: https://doi.org/10.3390/mi13010010.

[12] "Chapter 6 - ELLIPSOMETRIC CHARACTERIZATION OF THIN FILMS".
M. Fried, T. Lohner, and P. Petrik. In: *Handbook of Surfaces and Interfaces of Materials*.
Ed. by Hari Singh Nalwa. Burlington: Academic Press, 2001, pp. 335–367.
ISBN: 978-0-12-513910-6. DOI: https://doi.org/10.1016/B978-012513910-6/50052-9.
URL: https://www.sciencedirect.com/science/article/pii/B9780125139106500529.

[13] "Harvesting blue energy using porous silicon". Romain Hanus. Prom. : Francis, Laurent.
PhD thesis. UCL - Ecole Polytechnique de Louvain, 2020.
URL: https://hdl.handle.net/2078.2/15361.

[14] "A comprehensive review on the synthesis and applications of ion exchange membranes".
Shanxue Jiang et al. In: *Chemosphere* 282 (2021), p. 130817. ISSN: 0045-6535.
DOI: https://doi.org/10.1016/j.chemosphere.2021.130817.
URL: https://www.sciencedirect.com/science/article/pii/S0045653521012881.

[15] *Porous silicon*. Farshid Karbassian. Apr. 2018. DOI: 10.5772/intechopen.72910.
URL: https://www.intechopen.com/chapters/58683.

[16] *Porous silicon*. Farshid Karbassian. Apr. 2018. DOI: 10.5772/intechopen.72910.
URL: https://www.intechopen.com/chapters/58683.

[17] "Precision size and refractive index analysis of weakly scattering nanoparticles in polydispersions". Anna D. Kashkanova et al. In: *Nature Methods* 19.5 (May 2022), pp. 586–593.
DOI: 10.1038/s41592-022-01460-z.
URL: https://pmc.ncbi.nlm.nih.gov/articles/PMC9119850/.

[18] "Nanoporous silicon flakes as anode active material for lithium-ion batteries".
Young-You Kim, Jeong-Hwa Lee, and Han-Jung Kim.
In: *Physica E: Low-dimensional Systems and Nanostructures* 85 (2017), pp. 223–226.
ISSN: 1386-9477. DOI: https://doi.org/10.1016/j.physe.2016.09.007.
URL: https://www.sciencedirect.com/science/article/pii/S1386947716304052.

[19] "Investigation of non-specific signals in nanoporous flow-through and flow-over based sensors".
Neeraj Kumar et al. In: *The Analyst* 139.6 (Dec. 2013), p. 1345. DOI: 10.1039/c3an01996a.
URL: https://pubs.rsc.org/en/content/articlelanding/2014/an/c3an01996a.

[20] "Porous Silicon Formation by Electrochemical Etching".
Orest Kuntyi, Galyna Zozulya, and Mariana Shepida.
In: *Advances in Materials Science and Engineering* 2022.1 (2022), p. 1482877.
DOI: https://doi.org/10.1155/2022/1482877.
URL: https://onlinelibrary.wiley.com/doi/abs/10.1155/2022/1482877.

[21] "Mesoporous Silica-Based materials for Electronics-Oriented applications".
Lukasz Laskowski et al. In: *Molecules* 24.13 (June 2019), p. 2395.
DOI: 10.3390/molecules24132395. URL: https://doi.org/10.3390/molecules24132395.

[22] "Elaboration and Light Emission Properties of Low Doped p-Type Porous Silicon Microcavities". G. Lérondel, P. Ferrand, and R. Romestain.
In: *MRS Online Proceedings Library* 452.1 (1996), pp. 711–716. ISSN: 1946-4274.
DOI: 10.1557/PROC-452-711. URL: https://doi.org/10.1557/PROC-452-711.

[23] "Hydrogen in porous silicon - A review". A.I. Manilov and V.A. Skryshevsky.
In: *Materials Science and Engineering: B* 178.15 (2013), pp. 942–955. ISSN: 0921-5107.
DOI: https://doi.org/10.1016/j.mseb.2013.05.001.
URL: https://www.sciencedirect.com/science/article/pii/S0921510713001761.

[24] "Porous silicon a useful imperfection". George Marsh.
In: *Materials Today* 5.1 (2002), pp. 36–41. ISSN: 1369-7021.
DOI: https://doi.org/10.1016/S1369-7021(02)05141-6.
URL: https://www.sciencedirect.com/science/article/pii/S1369702102051416.

[25] *Dielectric or Bragg mirrors. Hot, cold, and dichroic mirror. Request a quote.* Omega Optical. July 2024. URL: https://omega-optical.com/blog/dielectric-bragg-mirrors/.

[26] "Transport mechanisms in electrodialysis: The effect on selective ion transport in multi-ionic solutions". Selin Ozkul et al. In: *Journal of Membrane Science* 665 (2023), p. 121114.
ISSN: 0376-7388. DOI: https://doi.org/10.1016/j.memsci.2022.121114.
URL: https://www.sciencedirect.com/science/article/pii/S0376738822008596.

[27] "Prospects in Broadening the Application of Planar Solution-Based Distributed Bragg Reflectors". Emilia Palo and Konstantinos S. Daskalakis.
In: *Advanced Materials Interfaces* 10.19 (2023), p. 2202206.
DOI: https://doi.org/10.1002/admi.202202206.
URL: https://advanced.onlinelibrary.wiley.com/doi/abs/10.1002/admi.202202206.

[28] "Thermal oxidation of porous silicon: Study on reaction Kinetics". Andrea Edit Pap et al.
In: *The Journal of Physical Chemistry B* 108.34 (Aug. 2004), pp. 12744–12747.
DOI: 10.1021/jp049323y. URL: https://doi.org/10.1021/jp049323y.

[29] "A new process for the manufacturing of reproducible mesoporous silicon membranes". Tristan Pichonat and Bernard Gauthier-Manuel.
In: *Journal of Membrane Science* 280.1 (2006), pp. 494–500. ISSN: 0376-7388.
DOI: https://doi.org/10.1016/j.memsci.2006.02.010.
URL: https://www.sciencedirect.com/science/article/pii/S0376738806001281.

[30] "Refractiveindex.info database of optical constants". Mikhail N. Polyanskiy.
In: *Scientific Data* 11.1 (Jan. 2024). DOI: 10.1038/s41597-023-02898-2.
URL: https://doi.org/10.1038/s41597-023-02898-2.

[31] "Household aluminum foil matte and bright side reflectivity measurements: Application to a photobioreactor light concentrator design". Victor Pozzobon et al.
In: *Biotechnology Reports* 25 (2020), e00399. ISSN: 2215-017X.
DOI: https://doi.org/10.1016/j.btre.2019.e00399.
URL: https://www.sciencedirect.com/science/article/pii/S2215017X1930373X.

[32] "Porosity and roughness determination of porous silicon thin films by genetic algorithms". C.F. Ramirez-Gutierrez, J.D. Castaño-Yepes, and M.E. Rodriguez-Garcia.
In: *Optik* 173 (2018), pp. 271–278. ISSN: 0030-4026.
DOI: https://doi.org/10.1016/j.ijleo.2018.08.019.
URL: https://www.sciencedirect.com/science/article/pii/S0030402618311380.

[33] *Stable porous silicon-based optical sensing platform towards detection of bacterial lysis.* Jonathan Rasson. Apr. 2018.
URL: https://dial.uclouvain.be/pr/boreal/object/boreal:198385.

[34] Avantes, July 2025.
URL: https://www.avantes.com/products/accessories/reference-tiles/.

[35] "Porous Silicon in Practice. Preparation, Characterization and applications". Michael J. Sailor.
In: *Chromatographia* 76.11-12 (Mar. 2013), p. 721. DOI: 10.1007/s10337-013-2453-3.
URL: https://doi.org/10.1007/s10337-013-2453-3.

[36] "Dielectric permittivity of porous SI for use as substrate material in SI-Integrated RF devices". Panagiotis Sarafis, Emmanouel Hourdakis, and Androula G. Nassiopoulou. In: *IEEE Transactions on Electron Devices* 60.4 (Mar. 2013), pp. 1436–1443. DOI: 10.1109/ted.2013.2247042. URL: https://doi.org/10.1109/ted.2013.2247042.

[37] *Applications of effective medium theories in the Terahertz regime*. Maik Scheller, Christian Jansen, and Martin Koch. Jan. 2010. DOI: 10.5772/6915. URL: http://www.intechopen.com/books/recent-optical-and-photonic-technologies/applications-of-effective-medium-theories-in-the-terahertz-regime.

[38] "Temperature effect on the roughness of the formation interface of p-type porous silicon". S. Setzu, G. Lérondel, and R. Romestain. In: *Journal of Applied Physics* 84.6 (Sept. 1998), pp. 3129–3133. ISSN: 0021-8979. DOI: 10.1063/1.368467. URL: https://doi.org/10.1063/1.368467.

[39] Accessed: 08/2025. Thorlabs. Thorlabs.com, 2016. URL: https://www.thorlabs.com/catalogpages/obsolete/2016/SLS201_M.pdf.

[40] "A Mini-Review on Reflectins, from Biochemical Properties to Bio-Inspired Applications". Junyi Song et al. In: *International Journal of Molecular Sciences* 23.24 (2022). ISSN: 1422-0067. DOI: 10.3390/ijms232415679. URL: https://www.mdpi.com/1422-0067/23/24/15679.

[41] "Chemical and Biological Applications of Porous Silicon Technology". M. P. Stewart and J. M. Buriak. In: *Advanced Materials* 12.12 (2000), pp. 859–869. DOI: https://doi.org/10.1002/1521-4095(200006)12:12<859::AID-ADMA859>3.0.CO;2-0. URL: https://advanced.onlinelibrary.wiley.com/doi/abs/10.1002/1521-4095%28200006%2912%3A12%3C859%3A%3AAID-ADMA859%3E3.0.CO%3B2-0.

[42] *2460 SourceMeterő SMU instrument*. Tektronix. Accessed: 11 Aug. 2025. URL: https://www.tek.com/en/datasheet/2460-source-measure-unit.

[43] "Fabrication of porous silicon based tunable distributed Bragg reflectors by anodic etching of irradiated silicon". V.S. Vendamani et al. In: *Nuclear Instruments and Methods in Physics Research Section B: Beam Interactions with Materials and Atoms* 358 (2015), pp. 105–111. ISSN: 0168-583X. DOI: https://doi.org/10.1016/j.nimb.2015.05.040. URL: https://www.sciencedirect.com/science/article/pii/S0168583X15005352.

[44] "Porous silicon membranes and their applications: Recent advances". Roselien Vercauteren et al. In: *Sensors and Actuators A Physical* 318 (Dec. 2020), p. 112486. DOI: 10.1016/j.sna.2020.112486. URL: https://doi.org/10.1016/j.sna.2020.112486.

[45] "One-dimensional porous silicon photonic crystals for chemosensors: Geometrical factors influencing the sensitivity". Jackelyne L.M. Villanueva, Danilo.R. Huanca, and Adhimar F. Oliveira. In: *Sensors and Actuators A: Physical* 364 (2023), p. 114784. ISSN: 0924-4247. DOI: https://doi.org/10.1016/j.sna.2023.114784. URL: https://www.sciencedirect.com/science/article/pii/S0924424723006337.

[46] "SciPy 1.0: Fundamental Algorithms for Scientific Computing in Python". Pauli Virtanen et al. In: *Nature Methods* 17 (2020), pp. 261–272. DOI: 10.1038/s41592-019-0686-2.

[47] *Stable porous silicon membranes for biosensing*. Clara Whyte Ferreira. Prom. : Francis, Laurent. 2021. URL: http://hdl.handle.net/2078.1/thesis:30696.

[48] "Multifunctional mesoporous silica nanoparticles for biomedical applications". Bolong Xu et al. In: *Signal Transduction and Targeted Therapy* 8.1 (Nov. 2023). DOI: 10.1038/s41392-023-01654-7. URL: https://www.nature.com/articles/s41392-023-01654-7.

[49] "Distributed Bragg Reflectors for GaN-Based Vertical-Cavity Surface-Emitting Lasers". Cheng Zhang, Rami ElAfandy, and Jung Han. In: *Applied Sciences* 9.8 (2019). ISSN: 2076-3417. DOI: 10.3390/app9081593. URL: https://www.mdpi.com/2076-3417/9/8/1593.

[50] "Flow-Through porous silicon membranes for Real-Time Label-Free biosensing". Yiliang Zhao et al. In: *Analytical Chemistry* 88.22 (Oct. 2016), pp. 10940–10948. DOI: 10.1021/acs.analchem.6b02521. URL: https://doi.org/10.1021/acs.analchem.6b02521.

[51] "High-Sensitivity detection of changes in local refractive index and absorption by analyzing WGM microlaser emission via a 2D dispersion spectrometer". Xuewen Zhou, Malte C. Gather, and Giuliano Scarcelli. In: *ACS Photonics* 11.1 (Dec. 2023), pp. 267–275. DOI: 10.1021/acsphotonics.3c01448. URL: https://doi.org/10.1021/acsphotonics.3c01448.

UNIVERSITÉ CATHOLIQUE DE LOUVAIN
École polytechnique de Louvain
Rue Archimède, 1 bte L6.11.01, 1348 Louvain-la-Neuve, Belgique | **www.uclouvain.be/epl**